

Human neutrophils produce antifungal extracellular vesicles against *Aspergillus fumigatus*

Running Title: Human neutrophils produce antifungal EVs

Iordana A. Shopova^{1,2}, Ivan Belyaev^{3,9}, Prasad Dasari⁴, Susanne Jahreis⁵, Maria C. Stroe^{1,2}, Zoltán Cseresnyés³, Anna Medyukhina³, Carl-Magnus Svensson³, Thomas Krüger², Viktória Szeifert⁶, Sandor Nietzsche⁷, Theresia Conrad⁸, Olaf Kniemeyer², Marie von Lilienfeld-Toal⁵, Peter F. Zipfel^{1,4}, Erzsébet Ligeti⁶, Marc Thilo Figge^{3,9}, and Axel A. Brakhage^{1,2*}

¹Institute for Microbiology, Friedrich Schiller University, Jena, Germany

²Department of Molecular and Applied Microbiology, Leibniz Institute for Natural Product Research and Infection Biology (HKI), Jena, Germany

³Research Group Applied Systems Biology, Leibniz Institute for Natural Product Research and Infection Biology (HKI), Jena, Germany

⁴Department of Infection Biology, Leibniz Institute for Natural Product Research and Infection Biology (HKI), Jena, Germany

⁵Clinic of Internal Medicine II, Haematology and Oncology, University Hospital Jena, Germany,

⁶Department of Physiology, Semmelweis University, Budapest, Hungary,

⁷Centre for Electron Microscopy, Friedrich Schiller University, Jena, Germany

⁸Research Group Systems Biology and Bioinformatics, Leibniz Institute for Natural Product Research and Infection Biology (HKI), Jena, Germany

⁹Friedrich Schiller University, Jena, Germany

27 *corresponding author:

28 Axel A. Brakhage, Institute for Microbiology, Friedrich Schiller University Jena,

29 Leibniz Institute-HKI, Adolf-Reichwein-Str. 23, 07745 Jena, Germany

30 Email: axel.brakhage@uni-jena.de

31 Phone: +49 (0)3641 532 1001; +49 (0)3641 532 0802

32

33

34

Summary

Polymorphonuclear granulocytes (PMNs) are indispensable for controlling life-threatening fungal infections. In addition to various effector mechanisms, PMNs also produce extracellular vesicles (EVs). Their contribution to antifungal defense has remained unexplored. We reveal that the clinically important human pathogenic fungus *Aspergillus fumigatus* triggers PMNs to release a distinct set of antifungal EVs (afEVs). Proteome analyses indicated that afEVs are enriched in antimicrobial proteins. The cargo and release kinetics of afEVs are modulated by the fungal strain confronted. Tracking of produced afEVs indicated that they associated with fungal cells and even entered fungal hyphae, resulting in alterations in the morphology of the fungal cell wall, and imparted antifungal effects dose-dependently. Two identified human proteins of afEVs, cathepsin G and azurocidin, were heterologously expressed in fungal hyphae, which led to reduced fungal growth. In conclusion, the production of afEVs by PMNs offers an intriguing, previously overlooked mechanism of antifungal defense against *A. fumigatus*.

Introduction

Clinical management of invasive aspergillosis (IA), a severe systemic infection caused by the ubiquitous saprophytic fungus *Aspergillus fumigatus*, is a challenging endeavor. IA is characterized by high mortality rates related to the lack of early diagnosis, the occurrence of fungal resistance, and the lack of novel antifungal therapies (Dagenais and Keller, 2009; Kosmidis and Denning, 2015; Maertens et al., 2016; Marr et al., 2015; Osheroov and Kontoyiannis, 2017; Patterson et al., 2016). IA can occur in patients with congenital or therapy-induced myeloid cell defects, whereas healthy individuals that continuously inhale fungal spores (conidia; 2-3 μ m),

usually remain symptom-free. Data from neutropenic mice and patients have shown that polymorphonuclear granulocytes (PMNs) are indispensable for antifungal defense (Alflen et al., 2017; Bianchi et al., 2009; Bianchi et al., 2011; Bonnett et al., 2006; Dragonetti et al., 2017; Espinosa et al., 2017; Kalleda et al., 2016; Matute et al., 2009; Mircescu et al., 2009; Shlezinger et al., 2017); however, the exact mechanism of PMN-dependent fungal killing remains unresolved.

PMNs orchestrate immune surveillance against pathogenic fungi *via* oxidative burst (Boyle et al., 2011; Boyle et al., 2012; Shlezinger et al., 2017), degranulation (Levitz and Farrell, 1990; Zarembek et al., 2007), phagocytosis (Braem et al., 2015), cytokine release (Kalleda et al., 2016), and extracellular trap formation (Bianchi et al., 2009; Bianchi et al., 2011; Bruns et al., 2010; McCormick et al., 2010). Neutrophil extracellular traps (NETs) are only slightly fungistatic, and this alone does not explain the full antifungal activity of PMNs (Bruns et al., 2010; McCormick et al., 2010). In addition to these effector mechanisms, PMNs also produce PMN-derived extracellular vesicles (PMN EVs), which represent extracellular phosphatidylserine-containing microparticles (50 nm to 1 μ m) that elicit pleiotropic immunomodulatory effects in recipient immune and host cells (Eken et al., 2008; Eken et al., 2013; Gasser et al., 2003; Majumdar et al., 2016; Pliyev et al., 2014). PMN EVs serve many functions *in vivo* (Headland et al., 2015) (Gasser and Schifferli, 2005; Nieuwland et al., 2000; Watanabe et al., 2003) including antibacterial (Hess et al., 1999; Rossaint et al., 2016; Timar et al., 2013) and antiviral (Lim et al., 2015) defense and have been used as diagnostic markers for sepsis (Herrmann et al., 2015).

In this manuscript, we demonstrate the immune functionality of PMN EVs to the important filamentous fungal pathogen *A. fumigatus*. We phenotypically characterize the EVs produced by PMNs in response to *A. fumigatus* infection and

further detail the properties, locations and antifungal effects of these EVs on the fungus.

Results

PMNs release EVs in response to *A. fumigatus* infection

The role of EVs in antifungal defense remains unexplored. As such, we enriched and characterized PMN EVs produced from viable PMNs (>95% purity, >98% viability) during infection with opsonized wild-type (wt) *A. fumigatus* conidia (Figure S1A). To limit PMN apoptosis and subsequent production of apoptotic bodies (APB), we first determined the apoptotic fate of PMNs over the course of interaction with *A. fumigatus* by monitoring propidium iodide (PI) exclusion and Annexin V (AnnV) staining of cells (Figure 1A). In addition, we measured the release of APBs (AnnV⁺/PI⁺ EVs) by flow cytometry (Figure 1A, Figure S1B-E). Coincubation of human PMNs with fungi for 4 h, at a multiplicity of infection (MOI) of 5 conidia : 1 PMN, triggered minimal cell death in the PMN population (<10%) and limited APB release compared to an MOI of 10:1 (Figure 1A). Only about 3% of unstimulated PMNs underwent apoptosis (Figure 1B). An MOI of 5:1 was thus used throughout the remainder of the study to phenotypically characterize PMN EVs.

We were particularly interested in the previously-described, phosphatidylserine-containing fraction of EVs linked to host immunity, which could be interrogated by flow cytometry (Eken et al., 2008; Eken et al., 2013; Gasser et al., 2003; Majumdar et al., 2016; Pliyev et al., 2014). Labeling of EVs with cell surface maturation markers for the α -chain of the integrin receptor CR3 (CD11b) and the tetraspanin CD63 revealed an increase in the populations of antifungal EVs (afEVs) in response to infection relative to spontaneously released EVs (sEVs; Figure 1C-E, Figure S1F, G and Figure S2A-B). When we compared afEV formation induced by

stimulation of PMNs with wt and *pksP* mutant conidia, which lack the pigment and virulence determinant dihydroxynaphthalene (DHN) melanin (Eken et al., 2013; Jahn et al., 2000; Jahn et al., 2002; Tsai et al., 1998), we discovered that melanin-deficient conidia doubled the production of afEVs (Figure 1C-E), suggesting that fewer afEVs are produced against melanized wt conidia. We defined antifungal EVs induced by wt conidia as wt afEVs and antifungal EVs induced by *pksP* mutant conidia as *pksP* afEVs. Despite this major difference in afEV production, PMN viability was similar for wt and *pksP* mutant conidia-infected cells (Figure S2C); however, *pksP* conidia did exhibit higher opsonization (Tsai et al., 1998). The vesicular nature of the detected EVs was verified by detergent treatment using 1% (v/v)-Triton X-100, which led to the disappearance of signals for both AnnV and EV surface marker staining (Figure S1F, G). Cryo-transmission electron microscopy (TEM) imaging (Figure 1F-M) confirmed a heterogeneous population of circular structures with lipid bilayers for both afEVs and sEVs (Gasser et al., 2003; Yanez-Mo et al., 2015). Both types of EVs appeared to contain cargo with different spatial organization (Figure 1G-I, K-M), including practically empty EVs (Figure 1G, K) granular structure (Figure 1H, L) and homogenous distribution of cargo (Figure 1I, M).

afEVs are enriched for antimicrobial proteins

We next addressed the cargo of EVs in response to infection. We purified proteins from afEVs (wt or *pksP* infected PMNs) and sEVs. Equal amounts of protein were labelled with tandem mass tags (TMT) or analyzed by label-free quantification (LFQ), followed by detection with nano-scale liquid chromatographic tandem mass spectrometry (nLC/MS-MS). We compared i) *pksP*- vs. wt-derived afEVs, ii) wt-derived afEVs vs. sEVs, and iii) *pksP*-derived afEVs vs. sEVs. Overlapping predictions for transmembrane domain proteins using three different tools (TMHMM

(Krogh et al., 2001), SignalP (Petersen et al., 2011), and WoLF PSORT (Horton et al., 2007)) identified 17 proteins in the TMT dataset and 29 proteins in the LFQ dataset (Table S1).

In comparison to sEVs, both wt and *pksP* afEVs contained a broader spectrum of proteins, and more importantly, higher amounts of antimicrobial peptides such as histones H2A, H2B, and H3.1, neutrophil elastase (NE), myeloperoxidase (MPO), cathepsin G, azurocidin, and defensin 1 (Table 1). CD11b and CD63 were enriched in afEVs compared to sEVs, thus confirming the flow cytometry data (Table 1, Figure 1D, E). In addition, afEVs contained higher amounts of metabolic enzymes involved in glycolysis such as glucose-6-phosphate isomerase and transketolase, the cell surface glycoprotein CD177, and F-actin. Proteins of the antimicrobial calprotectin complex (S100-A8, S100-A9) exhibited the highest absolute abundance in afEVs (Table S2, Table S3). Wt afEVs and *pksP* afEVs were more similar in protein content in comparison to sEVs (Table 1).

The comparison of the proteins from all EV subsets revealed that 60 proteins were shared between all groups, suggesting that these proteins are part of the core EV protein set. Gene ontology (GO)-term enrichment analysis of the 60 shared proteins revealed overrepresentation of proteins involved in Fc-γ receptor signaling, Arp2/3 complex-mediated actin nucleation, the IL-8 signaling pathway, cytoskeletal rearrangements, and positive regulation of actin polymerization (Figure 2). Infection with wt or *pksP* conidia led to formation of afEVs with distinct proteome cargos, characterized by increased levels of antimicrobial peptides and metabolic proteins. These findings suggested an antimicrobial function for afEVs.

afEVs influence fungal growth by inhibition of hyphal extension

To prove a potential antifungal activity of afEVs, we collected afEVs from PMNs stimulated with wt and *pksP* mutant conidia (wt afEVs and *pksP* afEVs, respectively), coincubated them in different concentrations with resting conidia, and monitored fungal growth by confocal laser scanning microscopy (CLSM; Figure S3A). The area of objects (single hyphae or clusters) was considered as the growth measure. The concentration of EVs was measured in “doses”. One dose of EVs was defined as the number of afEVs produced by 10^7 PMNs infected with *pksP* mutant conidia at 2 h post infection. At this time point, we found a relatively large amount of produced EVs (Figure 1C) associated with a relatively low fraction of APBs (Figure 1B). Doses for each condition were normalized according to abundance, from observations in Figure 1C. The wt afEVs generated by PMNs infected with wt conidia strongly inhibited the growth of wt and *pksP* hyphae in all donors when triple doses of EVs were applied (Figure 3A-D). These experiments revealed donor-heterogeneity in response to four different donors. Triple doses of *pksP* afEVs, as well as single doses of wt afEVs, were efficient in growth arrest of hyphal filaments in one donor only (Figure 3C). The fungistatic effects of afEVs for all donors were not due to delayed germination of conidia but rather resulted from the inhibition of hyphal extension (Figure 3E, F and Figure S3A, B). Interestingly, sEVs had no impact on the growth of fungi (Figure 3G). Thus, PMNs produce tailored afEVs with distinct functional properties in response to co-incubation with *A. fumigatus*.

afEVs associate with and are internalized into fungal cells

As discussed above, we observed that afEVs are capable of arresting fungal growth. To study the interactions of afEVs with fungi, we collected three-dimensional (3D) confocal fluorescent image stacks of wt hyphae coincubated with wt afEVs and *pksP* hyphae coincubated with *pksP* afEVs after 20 h of incubation. We quantified the

interactions of afEVs and hyphae using 3D image analysis to evaluate the densities of EVs within calcofluor white (CFW) staining (inside) of hyphae (EV volume inside hyphae normalized to hyphae volume) compared to the corresponding EV densities outside hyphae. Densities of afEVs inside hyphae were significantly higher than afEV densities outside hyphae for both wt and *pksP* hyphal filaments (Figure 4A, Movie S1 and S2). The 3D image analysis of fluorescence signals revealed extensive binding of afEVs induced by conidia of both fungal strains to hyphae, despite interrogation of equal volumes of EVs and hyphae (Figure S3C, D).

We further assessed the ability of wt afEVs to associate with hyphae by evaluating the volume of hyphae-associated EVs (HAEVs), which were defined as the sum of the volumes of afEVs bound to the cell wall or internalized into hyphae (Movies S1 and S2). The ability of afEVs to associate with hyphae was mainly dependent on the intrinsic properties of the donors' afEVs (Figure S3E), while the relative volume density of afEVs had a much smaller effect (Figure S3E-G). We next defined hyphae-associated DNA (HADNA) staining as PI⁺ signals colocalized with hyphae, which is indicative of hyphal cell damage. The amount of HADNA staining from hyphae incubated with afEVs was significantly higher than the amount of HADNA staining from control hyphae grown alone, as quantified by the HADNA positive volume normalized over the hyphae volume (Figure 4B, and Movie S2). The 3D image analysis also showed that PI⁺ staining of hyphae was associated with the interaction of HAEVs. In fact, more than 60% of the volume of PI⁺ hyphae were associated with HAEVs (Figure S3G and Movie S2). All donor EVs were capable of eliciting PI staining of hyphae, but the extent of this effect was donor dependent (Figure S3G). Our data imply that afEVs are fungistatic and appear to cause cell damage in a process likely associated with the physical interaction of hyphae and afEVs. In support of this finding, hyphae appear to undergo hyperbranching away

from the wt afEV layer in response to treatment (Movie S3), again suggesting antifungal activity.

The effect of afEVs on fungi led us to test for physical long-term alterations of cell wall morphology. To visualize these changes we obtained scanning electron microscopy (SEM) images of wt hyphae 50 h post wt afEV treatment. Treated hyphal filaments (Figure 4C) were again shorter, further confirming the antifungal nature of afEVs. Additional imaging showed slight alterations in the porousness of the cell surface, which included ruffling and invaginations that were not observed in hyphae grown without afEVs (Figure S4).

To further support our findings of afEVs in association with fungal cells, we performed 3D image analysis of wt afEV entry into GFP-expressing hyphae. The obtained data demonstrated that wt afEVs could be incorporated into the fungal cytoplasm (Figure 5A-D, Movie S2). Furthermore, we were able to differentiate four locations of EV-fungal interactions: i) the largest fraction of afEVs, 50-70%, (referred to as type I afEVs) were cell-wall associated EVs; ii) afEVs embedded into the cell wall amounted to 0.5-2.5% of EVs; iii) 15-45% of afEVs were found to be located at the interface between cell wall and cytoplasm; and iv) intracytoplasmic afEVs represented 0.2-3% of all afEVs (Figure 5A-D, Movie S2).

afEV proteins are toxic to fungal cells

We next assessed whether the antimicrobial proteins found in afEVs contribute to growth inhibition of hyphae when expressed heterologously in the fungus. The genes of two of these human proteins, cathepsin G and azurocidin, were placed under inducible expression in *A. fumigatus* hyphae (Figure S5A-C). Addition of the inducer, doxycycline, to cultures of the transgenic *A. fumigatus* strains (AfcathG and Afazuro) led to a massive growth reduction, further demonstrating that afEVs carry toxic cargo

(Figure 6A, B). The presence of the toxic human proteins in hyphae after induction with doxycycline was confirmed by LC-MS measurements of fungal protein extracts (Figure 6C).

Discussion

Neutrophils are critical for elimination of *A. fumigatus* from the human host (Gazendam et al., 2016); however, the exact extracellular mechanisms of how PMNs kill *A. fumigatus* hyphae are not known (Gazendam et al., 2016). *A. fumigatus*-triggered NETs are slightly fungistatic but do not account for the full activity of neutrophils (Bruns et al., 2010; McCormick et al., 2010). Here, we show that *ex vivo* applied human EVs triggered by conidia (afEVs) inhibit the growth of hyphae and elicit cell damage, adding a new mode of antifungal defense against *A. fumigatus*. We speculate that afEVs are produced primarily as a result of fungal-driven PMN activation, as APBs accounted for less than 5% of the total EV population.

afEV production was increased in response to *A. fumigatus* infection, as confirmed by flow cytometry. EVs increased with kinetics different from those previously reported for anti-*Staphylococcus aureus* PMN EVs, where maximum production was observed at 40 min (Timar et al., 2013). The interaction of PMNs with *A. fumigatus* conidia resulted in an enrichment of CD63 on afEVs, which was not observed in antibacterial EVs (Timar et al., 2013) and is typically only found on EVs smaller than 100 nm. afEVs were also enriched in MPO, NE, and cathepsin G, consistent with their antifungal function. Interestingly, and further supporting the importance of afEV cargo is the finding that cathepsin G, NE, and calprotectin knockout mice are all highly susceptible to infection with *A. fumigatus* (Bianchi et al., 2011; Tkalcovic et al., 2000).

Our results suggest that the cargo of afEVs is tailored to the pathogen, as wt and *pksP* conidia elicited different responses. It is important to note that the *pksP* mutant utilized in these studies is not a knockout, but instead derived from a UV-mutagenized strain (Langfelder et al., 1998). Previous work has indicated that the phenotypes observed with this strain are due to the inactivation of *pksP* and that they could be fully complemented by the wt *pksP* gene (Langfelder et al., 1998; (Tsai et al., 1998). Our findings also suggest a novel function for the fungal virulence factor DHN-melanin (Jahn et al., 1997; Langfelder et al., 2001) in modulating EV biogenesis and protein cargo. Melanized conidia are more poorly opsonized than non-melanized conidia, and as a consequence, show reduced phagocytosis by neutrophils, which might lead to lower afEV production (Tsai et al., 1998). This hypothesis is also supported by the observation that CD11b and CD63 receptors are differentially expressed on the surface of neutrophils during confrontation with *pksP* and wt conidia.

Our results demonstrate that afEVs associate with fungal hyphae and might be able to deliver their toxic cargo intracellularly. A recent study on the transit of intact amphotericin B packaged liposomes through the cell walls of *Candida albicans* and *Cryptococcus neoformans* supports the notion that in principle the fungal cell wall permits internalization of vesicles (Walker et al., 2018). Since human neutrophils cannot be genetically manipulated, we overcame this limitation in part by producing the afEV proteins cathepsin G and azurocidin in *A. fumigatus* using an inducible promoter system. The production of these proteins in the fungus clearly led to a massive growth defect, suggesting that delivery of these cargos could contribute to antifungal activity. In addition, we observed that fungal hyphae move away from afEVs by hyperbranching, suggesting that the fungus actively avoids afEVs. This

finding is consistent with other observations of hyperbranching away from neutrophils during infection (Ellett et al., 2017).

Our 3D image analysis revealed the potential of afEVs to induce fungal cell damage, while also revealing striking donor-dependence on afEV incorporation into hyphae and their fungistatic efficiency. The importance of PMN-generated reactive oxygen species (ROS) in induction of fungal cell death was recently demonstrated (Shlezinger et al., 2017). Whether afEVs, which contain subunits of NADPH oxidase, might contribute to this mechanism requires further investigation. Consistently, our data showed that the intracellular release of antimicrobial peptides could contribute to a severe inhibition of fungal growth.

In conclusion, our results suggest that human PMNs release afEVs in response to an *A. fumigatus* infection. These EVs contain a cargo of antimicrobial proteins that inhibit hyphal growth. We envision that the analysis of EVs produced in bronchoalveolar lavage-fluid represents a potentially useful tool for diagnostic and/or prognostic markers of IA. Although we hypothesize that afEVs serve as an important factor in the control of pathogenesis during *A. fumigatus* infection, much work remains to completely unveil the function of these important intercellular mediators.

METHODS

Ethics statement

This study was approved by the Institutional Review Board of the Jena University Hospital (approval number: 2395-10/08 and 5074-02/17) in agreement with the Declaration of Helsinki.

Strains, growth conditions, and fungal biomass determination

A. fumigatus ATCC 46645, the GFP-expressing strain AfS148 (Lothar et al., 2014), and the melanin-free *pksP* mutant (Langfelder et al., 1998) were maintained on malt extract (Sigma-Aldrich) agar plates supplemented with 2% (w/v) agar for 5 days at 37°C. When appropriate, *A. fumigatus* ATCC 46645 and the overexpression strains *A. fumigatus* Afazuro and AfcathG were cultivated on *Aspergillus* Minimal Medium (AMM) for 3 days at 37°C, as described (Weidner et al., 1998). All conidia were harvested in sterile deionized water, filtered through 40 µm cell strainers (BD Biosciences, Heidelberg, Germany), washed, and resuspended in deionized sterile water. Spore suspensions were counted in a Thoma chamber and stored at 4°C for no longer than 1 week. Freshly harvested spore suspensions were used for each experiment.

For biomass determination, 10^8 conidia/ml were inoculated in 100 ml AMM, supplemented with or without 10 µg/ml doxycycline when needed for induction of tet^{ON} promoter, and grown at 37°C at 200 rpm for 24 h. Mycelia were collected, washed, filtered through Miracloth, and dried at 60°C for 3 days before weighing.

Opsonization of fungi

Fresh venous blood from adult male healthy volunteers, aged 20-35 years, was withdrawn after informed written consent and used for preparation of normal human serum (NHS). Volunteers had not taken any anti-inflammatory medications for >10 days and had not consumed alcohol for >3 days prior to donation. NHS was obtained by pooling serum prepared from fresh venous blood of seven healthy human donors. Serum was stored at -80°C until use. Conidia were opsonized in 50% (v/v) NHS and 50% (v/v) Hank's balanced salt solution (HBSS) (HyClone, GE Healthcare) for 1 h at 37°C at 500 rpm in duplicate. Conidia were pelleted by centrifugation at $16,000 \times g$ at 4°C for 10 min and subsequently washed three times with HBSS prior to

confrontation assays with PMNs. Conidia were pelleted by centrifugation at 16,000 × *g* at 4°C for 10 min and subsequently washed three times with HBSS prior to confrontation assays with PMNs.

PMN isolation

PMNs were isolated from fresh venous blood of healthy adult volunteers with purity above 95% and viability at 98% as described in detail (Gasser et al., 2003) with slight modifications as follows: blood was collected in K₂EDTA BD Vacutainer tubes (BD Biosciences) and Biocoll Separation Solution (Biochrom, GE Healthcare) was used for gradient centrifugation. Neutrophil purity was determined using an antibody cocktail as follows: CD3-PE (clone SK7; dilution 1:50), CD14-V500 (M5E2; 1:200), CD16-APC-Cy7 (3G8; 1:50), CD19-AF700 (cloneHIB19; 1:100), CD56-FITC (NCAM16.2; 1:100), and CD66b-PerCP-Cy5.5 (G10F5; 1:66) obtained from BD Pharmingen and CCR3-APC (5E8; 1:40) from Biolegend. Cells (1×10⁶) were blocked with 5% (v/v) mouse serum and then stained for CCR3 for 10 min at 37°C. Subsequently, an antibody cocktail mix was applied for staining of the remaining antigens from the above mentioned panel for an additional 30 min at RT. For cell damage assays at each time point, 2×10⁶ neutrophils in 200 µl of HBSS were incubated with PI (5 µg) and Alexa 647-AnnV (5 µl) for 15 min at RT. Then, the cells were centrifuged at 400 × *g* for 5 min and resuspended in 500 µl Dulbecco's phosphate buffer saline (DPBS). Fluorescence of 10⁴ gated neutrophils was measured by flow cytometry with a BD LSR II (BD Biosciences) using BD FACSDiva Software Version 8.0.1 (BD Bioscience). Data were analyzed with FlowJo software.

EV isolation and characterization

EVs were prepared following a procedure by Timar *et al.* (Timar et al., 2013) with slight modifications. PMNs with a density of 1×10^7 cell/ml were confronted with opsonized wt *A. fumigatus* ATCC 46645 or opsonized *A. fumigatus pksP* mutant conidia with an MOI of 10:1 or 5:1 in HBSS with Ca^{2+} and Mg^{2+} (HyClone, GE Healthcare) on a linear shaker (100 rpm) at 37°C for 4 h. EVs produced by uninfected PMNs (spontaneous (s)EVs) served as negative control. At the selected incubation time points, PMNs were sedimented for 10 min with $1000 \times g$ at 4°C on 45° fixed-angle rotor FA-45-30-11 (Eppendorf). The supernatant was filtered by gravity through sterile PVDF 5.0 μm Millex syringe filters (Merck-Millipore). EV suspensions were stained with a cocktail of fluorescence-conjugated mAbs (PerCP/Cy5.5-anti-human-CD63, clone H5C6 from Biolegend; RPE-CD11b from Dako; and FITC-Annexin V from Biolegend) for 20 min at RT and centrifuged on 45° fixed angle rotor FA-45-30-11 (Eppendorf) for 20 min, 4°C, $19,500 \times g$. Corresponding single-stained Ab isotype controls were also prepared (PerCP/Cy5.5 mouse IgG1, κ isotype (MOPC-21) from Biolegend; mouse IgG1, κ isotype RPE-CD11b from Dako). After centrifugation the supernatant was carefully aspirated and EV pellets were resuspended in the original incubation volume in HBSS.

The size distribution of PMN EVs was recorded with a Nanotracs Flex 180° dynamic light scattering system (Microtrack) at 22°C. At least 20 measurements per sample were performed and the average hydrodynamic radius was calculated with the sphere approximation using the FLEX11 software.

Flow cytometry measurements of EVs were conducted on BD LSR Fortessa using the BD FACs Diva Software Version 8.0.1 (BD Biosciences) applying an optimized EV flow protocol (Lorincz et al., 2014). Briefly, pure HBSS was used to record instrument noise. The upper size limit detection threshold was set by fluorescent rainbow particles with mid-range intensity and size 3.0-3.4 μm

(Biolegend) resuspended in HBSS. Stained EV suspensions were enumerated in the fluorescent gate above the gate of the negative isotype-labelled controls. Once measured, samples were treated with 1% (v/v) Triton X-100 to verify the vesicular nature of the detected events. Detergent-resistant events (false positives) were subtracted from the total measured events using the FlowJo version 10.0.7 from Tree Star software.

Imaging techniques (Cryo-TEM, SEM, and CLSM)

For ultrastructural investigations isolated EVs were imaged with cryo transmission electron microscopy (cryo-TEM) and EV effects on fungi were studied with scanning electron microscopy (SEM). Confocal laser scanning microscopy (CLSM) was used to image the growth of *A. fumigatus* under various conditions.

For cryo-TEM imaging sEVs and wt afEVs collected at a time point of 2 h were freshly prepared using neutrophils from the same male donor and immediately subjected to imaging. 5 µl of purified pelleted EVs in HBSS were applied to carbon-coated copper grids (R1.2/1.3, Quantifoil Micro Tools GmbH) and the excess of liquid was blotted automatically for two seconds from the reverse side of the grid with a strip of filter paper. Subsequently, the samples were rapidly plunged into liquid ethane (cooled to -180°C) in a cryobox (Carl Zeiss NTS GmbH). Excess ethane was removed with a piece of filter paper. The samples were transferred with a cryo-transfer unit (Gatan 626-DH) into the pre-cooled cryo-TEM (Philips CM 120) operated at 120 kV and viewed under low dose conditions. The images were recorded with a 2k CMOS Camera (F216, TVIPS, Gauting).

SEM analysis was used to investigate the effect of afEVs on the growth of *A. fumigatus*. Therefore, wt conidia were coincubated with 3x dose of PMN EVs for 50 h in HBSS at 37°C in the dark. At the end of the coincubation time, samples were fixed

in 2.5% (v/v) glutaraldehyde in HBSS on IsoporeTM membrane TMTP filters with pore size 5 μ m (Merck-Millipore) for 30 min followed by washing thrice with HBSS buffer (10 min each). Then, the samples were dehydrated in ascending ethanol concentrations (30, 50, 70, 90, and 96% (v/v)) for 10 min each by thoroughly rinsing the membranes and soaking through the liquids with blotting paper. Subsequently, ethanol was changed with hexamethyldisilazane (Merck) in two steps (50%, 96% (v/v)), and samples were air-dried. Afterwards, the samples were sputter-coated with gold (thickness approx. 4 nm) using a SCD005 sputter coater (BAL-TEC, Liechtenstein) to avoid surface charging and investigated with a field emission (FE) SEM LEO-1530 Gemini (Carl Zeiss NTS GmbH).

LC-MS/MS-based proteome analysis of EVs

For proteome analysis of EVs, purified sEVs and afEVs generated against wt and *pksP* conidia were collected from a pool of 20 different donors in HBSS and stored at -80°C for no longer than 1 week prior to protein extraction. EV suspensions were concentrated on 3 kDa polyethersulfone (PES) membrane centrifugal filters (VWR International) for 5 min at 14,000 rpm at 4°C (Sigma 3-KIS centrifuge). Samples were snap-frozen in liquid N₂ and delipidated by protein precipitation based on the protocol of Wessel and Flügge (Wessel and Flugge, 1984). Proteins were resolubilized in 50 μ l 50 mM triethyl ammonium bicarbonate (TEAB) in 1:1 trifluoroethanol (TFE)/H₂O and denatured for 10 min at 90°C. Protein quantification was performed using the Direct Detect[®] system (Merck-Millipore). Each sample was set to 40 μ g of total protein in 100 μ l in 100 mM TEAB. Proteins were reduced with 10 mM tris(2-carboxyethyl) phosphine (TCEP) at 55°C for 60 min and alkylated with 12.5 mM iodoacetamide (IAA) at RT for 30 min in the dark. Proteins were digested for 2 h at 37°C with Lys-C and 16 h at 37°C with Trypsin Gold (both Promega). For TMT 6-plex

labeling (Thermo Fisher Scientific), digested peptides were treated according to the manufacturer's instructions. Labelled peptides were pooled and fractionated offline on HyperSep SCX (strong cation exchange) columns (Thermo Fisher Scientific).

LC-MS/MS analyses and protein database searches were performed as described in Baldin et al. (2015) with the following modifications: gradient elution of A (0.1% (v/v) formic acid in water) and B (0.1% (v/v) formic acid in 90/10 acetonitrile/water (v/v)) was as follows: 0-4 min at 4% B, 15 min at 5.5% B, 30 min at 7% B, 220 min at 12.5% B, 300 min at 17% B, 400 min at 26% B, 450 min at 35% B, 475 min at 42% B, 490 min at 51% B, 500 min at 60% B, 515-529 min at 96% B, 530-600 min at 4% B. Precursor ions were measured in full scan mode within a mass range of m/z 300-1500 at a resolution of 140k FWHM using a maximum injection time of 120 ms and an AGC (automatic gain control) target of 3×10^6 (TMT) or 1×10^6 (LFQ). The isolation width was set to m/z 0.8 (TMT) or 2.0 (LFQ) amu. Tandem mass spectra were searched by Proteome Discoverer (PD) 2.1 (Thermo Fisher Scientific Waltham) against the UniProt database of *Homo sapiens* (22/08/2016) using the algorithms of Mascot v2.4.1 (Matrix Science), Sequest HT and MS Amanda (Dorfer et al., 2014). Dynamic modifications were oxidation of Met (LFQ) and TMT-6-plex reaction at Tyr (not considered for quantification). Static modifications were carbamidomethylation of Cys by iodoacetamide (LFQ) and TMT-6-plex reaction at Lys and the peptide N-terminus. The TMT significance threshold for differentially produced proteins was set to factor ≥ 1.5 (up- or down-regulation). The data was further manually evaluated based on the average reporter ion count (≥ 2 for medium confidence, ≥ 4 for high confidence). Furthermore, the average variability was observed as a function of the differential regulation and the reporter ion count. Label-free quantification was performed by the Precursor Ions Area method of PD 2.1. The mass tolerance was set to 2 ppm and the signal-to-noise ratio had to be above 3. The

abundance values were normalized based on the total peptide amount. The significance threshold for differential protein abundance was set to factor ≥ 2.0 (up- or down-regulation). The mass spectrometry proteomics data have been deposited to the ProteomeXchange Consortium *via* the PRIDE partner repository with the dataset identifier PXD005994 (Vizcaino et al., 2016).

Functional annotation of the EV proteome

The dataset of differentially regulated proteins was filtered by the human serum proteome represented in Piper and Katzmann (2007) and in addition, by keratin, epidermal proteins and complement component 5 α , which were not considered for the proteome comparison. The filtering and the overlap analyses were performed in R using packages provided by Bioconductor (Ihaka and Gentleman, 1996). The GO-term enrichment analysis of the overlapping proteins of the TMT datasets was performed using FungiFun2 (Priebe et al., 2015). The results contain categories determined by Fisher's exact test and Benjamini-Hochberg corrected p-values below 0.05.

Analysis of heterologously expressed human azurocidin and cathepsin G

Protein preparation and LC-MS/MS analysis and database search for identification of proteins was essentially performed as previously described (Baldin et al., 2015) except the following changes: LC gradient elution was as follows: 0 min at 4% B, 5 min at 5% B, 30 min at 8% B, 60 min at 12% B, 100 min at 20% B, 120 min at 25% B, 140 min at 35% B, 150 min at 45% B, 160 min at 60 %B, 170-175 min at 96% B, 175.1-200 min at 4% B. Mass spectrometry analysis was performed on a QExactive HF instrument (Thermo) at a resolution of 120,000 FWHM for MS1 scans and 15,000 FWHM for MS2 scans. Tandem mass spectra were searched against the UniProt

database (2018/07/08, <https://www.uniprot.org/proteomes/UP000002530>) of *Neosartorya fumigata* (Af293) and the human protein sequences of azurocidin and cathepsin G, using Proteome Discoverer (PD) 2.2 (Thermo) and the algorithms of Sequest HT (version of PD2.2) and MS Amanda 2.0. Modifications were defined as dynamic Met oxidation and protein N-term acetylation as well as static Cys carbamidomethylation.

Determination of EV effects on fungi by CLSM

For determining EV effects on fungi, EVs were dosed according to cell equivalents. One EV dose was defined as the number of EVs produced by 10^7 PMNs infected with *pksP* mutant conidia at an MOI of 5:1 at 2 h post infection, which represented the maximal observed production of EVs (Fig. 1C). At this time point, *pksP* conidia stimulated double the afEVs as wt conidia and 12-fold more than sEVs from the same number of cells. Consequently, doses were adjusted to appropriately compare equal numbers of EVs. Freshly prepared and portioned EVs were coincubated with 30 μ l of a suspension of 10^6 conidia/ml in HBSS in 12-well chambers (Ibidi GmbH). A CLSM system, Zeiss LSM 780 (Carl Zeiss SAS), was employed; see Supplementary Methods S1 for details. Images were acquired once per hour from ten different fields of view per well in a microtiter plate. The 2D confocal images were recorded at 208 by 208 nm pixel size, whereas 3D image stacks had a voxel volume of 0.025 (19 samples) or 0.034 (15 samples) μ m³.

After 20 h, the samples were stained with Annexin-V FITC (1:60; Biolegend), PI (to a final concentration of 0.0167 μ g/ μ l) and CFW (to a final concentration of 0.167 μ g/ μ l) in order to assess EV entry into hyphae and to collect image Z-stacks by CLSM. When the *A. fumigatus*-GFP strain AfS148 was used, the staining cocktail

consisted of Annexin V-Alexa 647 and CFW, whereas PI staining was omitted in order to avoid spectral overlaps.

3D image analysis of EV internalization

For a quantitative analysis of the wt afEVs-hyphae interactions, the 3D shape of each object type was reconstructed based on 4D (3D plus color) fluorescence images using the following procedure: the images were deconvolved using HuygensPro (SVI, Hilversum, The Netherlands) with a measured PSF (see Supplementary Methods S1) that was recorded individually for each fluorescence channel. The deconvolved images were transferred to Imaris (Bitplane, Zürich, Switzerland) for 3D reconstruction. The basic object types (hyphae, DNA, EVs) were reconstructed in Imaris using manually adjusted templates. The reconstructed hyphae only included objects from the CFW channel (see Determination of EV effects on fungi by CLSM) that were larger than $20 \mu\text{m}^3$ and had no surface points on the sample border. The reconstruction process is presented in Movies S1-3. The control samples and those with GFP fluorescence were reconstructed using the same procedure. Hyphae-associated DNA (HADNA) and hyphae-associated EVs (HAEVs) were identified by using a binary mask of the hyphae (channel 4; Movie S2). Only those objects were assigned as hyphae-associated that were located either on the border or inside the hyphae, as identified by a threshold of the mean value of the CFW fluorescence signal being above 5×10^{-10} . The binary mask of HAEVs was used to select HADNA that interacted with EVs (HADNAi, mean value of binary mask of hyphae, Movie S2). Finally, the total volume of each object class at every field of view was computed. Additionally, the EV volume inside hyphae was computed over the regions that were double-positive for AnnV (EVs) and CFW (hyphae), whereas the EV volume outside

hyphae was defined as the volume that was positive for AnnV but not in CFW. EV densities inside and outside hyphae were then defined as follows:

$$\text{EV density inside} = \frac{\text{EV volume inside hyphae}}{\text{Hyphae volume}}$$

$$\text{EV density outside} = \frac{\text{EV volume outside hyphae}}{\text{Sample volume} - \text{Hyphae volume}}$$

The sample volume was estimated based on voxel size and number of voxels in each sample (automatically performed by Imaris).

Automated 2D image analysis of hyphal growth

For quantitative analysis of hyphal growth in bright field microscopy images, the area of the regions of interest (ROI) corresponding to the conidia and the hyphae, was computed automatically for each image. The image analysis algorithm was implemented in Matlab (Matlab 2017a, MathWorks). The code is available from the authors upon request. The procedure included: (1) binarization of image data, (2) binary image enhancement, (3) selection of ROI based on morphological filtering, (4) image post-processing and filtering, and (5) area measurement of the ROI, see Supplementary Methods S2 for details. Two of the original image sections, together with the resulting images after having applied the aforementioned steps, are illustrated in Fig. S3B. All parameters of the algorithm were adjusted to minimize the detection of noise and of out-of-focus objects, which was confirmed by visual inspection of the images.

Generation of transgenic *A. fumigatus* strains

For expression of the human azurocidin *AZU1* and cathepsin G *CTSG* genes in *A. fumigatus*, the tetracycline-controlled transcriptional activation (tet^{ON}) system was

used (Helmschrott et al., 2013). The human azurocidin and cathepsin G cDNA sequences obtained from the NCBI database were codon optimized for *A. fumigatus* using the GENEius Tool (<https://www.eurofinsgenomics.eu/en/gene-synthesis-molecular-biology/geneius/>) and synthesized (Eurofins Genomics). The genes were PCR-amplified using the Phusion Flash High-Fidelity PCR Master Mix (Thermo Fisher Scientific) with the primer pairs Azu_polictail_f and Azu_tetter_rev for azurocidin and cathG_polictail_f cathg_teftail_R for cathepsin G (Table S4). The tet^{ON}-system, together with the pyrithiamine resistance marker gene, was amplified from plasmid pSK562. The tet^{ON} cassette, the two genes with matching flanks, and the vector pYES2 were assembled by using the NEBuilder HiFi DNA Assembly Master Mix (New England Biolabs) according to the manufacturer's instructions. The assembled 10 kb plasmids were sequenced and subsequently used to transform *A. fumigatus* ATCC 46645 as previously described (Weidner et al., 1998). Transformants were selected with 0.1 µg/ml pyrithiamine.

Southern blot analysis to confirm genetic manipulation of *A. fumigatus* strains was carried out as described before (Unkles et al., 2014). For Northern blot analysis, 16-hour-old pre-cultures were treated with 10 µg/ml doxycycline. Mycelia were harvested 3 h post addition of doxycycline. RNA extraction and detection of RNA by Northern blot were carried out as previously described (Unkles et al., 2014).

Acknowledgements

We are thankful to all anonymous blood donors, to Ellen Ritter and Tobias Rachow (blood withdrawal), Frank Steiniger (cryo-TEM imaging), and Sven Krappmann (AfS148 strain, pSK562 plasmid). We thank Matthew Blango for the editorial input in the manuscript. This work was supported by the Collaborative Research Center/Transregio 124 'Pathogenic fungi and their human host - Networks of

interaction - FungiNet' funded by the Deutsche Forschungsgemeinschaft (DFG) (projects A1, B3, B4, C6, INF, Z2), the DFG-funded excellence graduate school Jena School for Microbial Communication (JSMC) and the Leibniz ScienceCampus *InfectoOptics* SAS-2015-HKI-LWC (Project BLOODi).

Author contributions

I.A.S. conceived, designed, and participated in performing all experiments and writing the manuscript. T.K. and O.K. performed proteome nLC-MS/MS analysis. P.D. performed flow cytometry studies on neutrophils. M.S. generated and characterized transgenic *A. fumigatus* strains. S.J. and V.S. performed flow cytometry of vesicles and/ or purity of neutrophils and analyzed raw flow cytometry data. Z.C. designed the confocal fluorescence microscopy experiments and participated in the CLSM imaging experiments. Z.C. and I.B. established and performed the 3D image analysis of vesicle internalization. I.B. and A.M. developed the algorithm for 2D image analysis of vesicle effects on fungal growth. A.M. and C.M.S. performed statistical analysis of the data and prepared data plots. S.N. conducted transmission electron microscopy. T.C. performed functional annotation of the proteomic data. A.A.B., M.L.T., E.L., P.F.Z., and M.T.F contributed to the design of the study, participated in data interpretation, and supervised the project. All authors wrote, edited and approved the manuscript.

Conflict of interest

The authors declare no conflict of interest.

References

620 Alfken, A., Prufer, S., Ebner, K., Reuter, S., Aranda Lopez, P., Scharrer, I., Banno, F.,
621 Stassen, M., Schild, H., Jurk, K., *et al.* (2017). ADAMTS-13 regulates neutrophil
622 recruitment in a mouse model of invasive pulmonary aspergillosis. *Sci Rep* 7, 7184.

623 Baldin, C., Valiante, V., Kruger, T., Schafferer, L., Haas, H., Kniemeyer, O., and
624 Brakhage, A.A. (2015). Comparative proteomics of a tor inducible *Aspergillus*
625 *fumigatus* mutant reveals involvement of the Tor kinase in iron regulation. *Proteomics*
626 15, 2230-2243.

627 Bianchi, M., Hakkim, A., Brinkmann, V., Siler, U., Seger, R.A., Zychlinsky, A., and
628 Reichenbach, J. (2009). Restoration of NET formation by gene therapy in CGD
629 controls aspergillosis. *Blood* 114, 2619-2622.

630 Bianchi, M., Niemiec, M.J., Siler, U., Urban, C.F., and Reichenbach, J. (2011).
631 Restoration of anti-*Aspergillus* defense by neutrophil extracellular traps in human
632 chronic granulomatous disease after gene therapy is calprotectin-dependent. *J*
633 *Allergy Clin Immunol* 127, 1243-1252.e1247.

634 Bonnett, C.R., Cornish, E.J., Harmsen, A.G., and Burritt, J.B. (2006). Early neutrophil
635 recruitment and aggregation in the murine lung inhibit germination of *Aspergillus*
636 *fumigatus* conidia. *Infect Immun* 74, 6528-6539.

637 Boyle, K.B., Gyori, D., Sindrilaru, A., Scharffetter-Kochanek, K., Taylor, P.R., Mocsai,
638 A., Stephens, L.R., and Hawkins, P.T. (2011). Class IA phosphoinositide 3-kinase
639 beta and delta regulate neutrophil oxidase activation in response to *Aspergillus*
640 *fumigatus* hyphae. *J Immunol* 186, 2978-2989.

641 Boyle, K.B., Stephens, L.R., and Hawkins, P.T. (2012). Activation of the neutrophil
642 NADPH oxidase by *Aspergillus fumigatus*. *Ann N Y Acad Sci* 1273, 68-73.

643 Braem, S.G., Rooijackers, S.H., van Kessel, K.P., de Cock, H., Wosten, H.A., van
644 Strijp, J.A., and Haas, P.J. (2015). Effective neutrophil phagocytosis of *Aspergillus*
645 *fumigatus* is mediated by classical pathway complement activation. J Innate Immun
646 7, 364-374.

647 Bruns, S., Kniemeyer, O., Hasenberg, M., Aimaganianda, V., Nietzsche, S., Thywissen,
648 A., Jeron, A., Latge, J.P., Brakhage, A.A., and Gunzer, M. (2010). Production of
649 extracellular traps against *Aspergillus fumigatus in vitro* and in infected lung tissue is
650 dependent on invading neutrophils and influenced by hydrophobin RodA. PLOS
651 Pathog 6, e1000873.

652 Dagenais, T.R., and Keller, N.P. (2009). Pathogenesis of *Aspergillus fumigatus* in
653 Invasive Aspergillosis. Clin Microbiol Rev 22, 447-465.

654 Dorfer, V., Pichler, P., Stranzl, T., Stadlmann, J., Taus, T., Winkler, S., and Mechtler,
655 K. (2014). MS Amanda, a universal identification algorithm optimized for high
656 accuracy tandem mass spectra. J Proteome Res 13, 3679-3684.

657 Dragonetti, G., Criscuolo, M., Fianchi, L., and Pagano, L. (2017). Invasive
658 aspergillosis in acute myeloid leukemia: Are we making progress in reducing
659 mortality? Med Mycol 55, 82-86.

660 Eken, C., Gasser, O., Zenhausern, G., Oehri, I., Hess, C., and Schifferli, J.A.
661 (2008). Polymorphonuclear neutrophil-derived ectosomes interfere with the
662 maturation of monocyte-derived dendritic cells. J Immunol 180, 817-824.

663 Eken, C., Sadallah, S., Martin, P.J., Treves, S., and Schifferli, J.A. (2013). Ectosomes
664 of polymorphonuclear neutrophils activate multiple signaling pathways in
665 macrophages. Immunobiology 218, 382-392.

666 Ellett, F., Jorgensen, J., Frydman, G.H., Jones, C.N., and Irimia, D. (2017).
667 Neutrophil Interactions Stimulate Evasive Hyphal Branching by *Aspergillus fumigatus*.
668 PLoS Pathog 13, e1006154.

669 Espinosa, V., Dutta, O., McElrath, C., Du, P., Chang, Y.J., Cicciarelli, B., Pitler, A.,
670 Whitehead, I., Obar, J.J., Durbin, J.E., *et al.* (2017). Type III interferon is a critical
671 regulator of innate antifungal immunity. Sci Immunol 2, pii: eaan5357.

672 Gasser, O., Hess, C., Miot, S., Deon, C., Sanchez, J.C., and Schifferli, J.A. (2003).
673 Characterisation and properties of ectosomes released by human polymorphonuclear
674 neutrophils. Exp Cell Res 285, 243-257.

675 Gasser, O., and Schifferli, J.A. (2005). Microparticles released by human neutrophils
676 adhere to erythrocytes in the presence of complement. Exp Cell Res 307, 381-387.

677 Gazendam, R.P., van de Geer, A., Roos, D., van den Berg, T.K., and Kuijpers, T.W.
678 (2016). How neutrophils kill fungi. Immunol Rev 273, 299-311.

679 Headland, S.E., Jones, H.R., Norling, L.V., Kim, A., Souza, P.R., Corsiero, E., Gil,
680 C.D., Nerviani, A., Dell'Accio, F., Pitzalis, C., *et al.* (2015). Neutrophil-derived
681 microvesicles enter cartilage and protect the joint in inflammatory arthritis. Sci Transl
682 Med 7, 315ra190.

683 Helmschrott, C., Sasse, A., Samantaray, S., Krappmann, S., and Wagener, J. (2013).
684 Upgrading fungal gene expression on demand: improved systems for doxycycline-
685 dependent silencing in *Aspergillus fumigatus*. Appl Environ Microbiol 79, 1751-1754.

686 Herrmann, I.K., Bertazzo, S., O'Callaghan, D.J., Schlegel, A.A., Kallepitis, C.,
687 Antcliffe, D.B., Gordon, A.C., and Stevens, M.M. (2015). Differentiating sepsis from

688 non-infectious systemic inflammation based on microvesicle-bacteria aggregation.
689 *Nanoscale* 7, 13511-13520.

690 Hess, C., Sadallah, S., Hefti, A., Landmann, R., and Schifferli, J.A. (1999).
691 Ectosomes released by human neutrophils are specialized functional units. *J*
692 *Immunol* 163, 4564-4573.

693 Horton, P., Park, K.J., Obayashi, T., Fujita, N., Harada, H., Adams-Collier, C.J., and
694 Nakai, K. (2007). WoLF PSORT: protein localization predictor. *Nucleic Acids Res* 35,
695 W585-587.

696 Ihaka, R., and Gentleman, R. (1996). R: a language for data analysis and graphics. *J*
697 *Comput Graph Stat* 5, 299-314.

698 Jahn, B., Boukhallouk, F., Lotz, J., Langfelder, K., Wanner, G., and Brakhage, A.A.
699 (2000). Interaction of human phagocytes with pigmentless *Aspergillus* conidia. *Infect*
700 *Immun* 68, 3736-3739.

701 Jahn, B., Koch, A., Schmidt, A., Wanner, G., Gehringer, H., Bhakdi, S., and
702 Brakhage, A.A. (1997). Isolation and characterization of a pigmentless-conidium
703 mutant of *Aspergillus fumigatus* with altered conidial surface and reduced virulence.
704 *Infect Immun* 65, 5110-5117.

705 Jahn, B., Langfelder, K., Schneider, U., Schindel, C., and Brakhage, A.A. (2002).
706 PKSP-dependent reduction of phagolysosome fusion and intracellular kill of
707 *Aspergillus fumigatus* conidia by human monocyte-derived macrophages. *Cell*
708 *Microbiol* 4, 793-803.

709 Kalleda, N., Amich, J., Arslan, B., Poreddy, S., Mattenheimer, K., Mokhtari, Z.,
710 Einsele, H., Brock, M., Heinze, K.G., and Beilhack, A. (2016). Dynamic immune cell

711 recruitment after murine pulmonary *Aspergillus fumigatus* infection under different
712 immunosuppressive regimens. Front Microbiol 7, 1107.

713 Kosmidis, C., and Denning, D.W. (2015). The clinical spectrum of pulmonary
714 aspergillosis. Thorax 70, 270-277.

715 Krogh, A., Larsson, B., von Heijne, G., and Sonnhammer, E.L. (2001). Predicting
716 transmembrane protein topology with a hidden Markov model: application to
717 complete genomes. J Mol Biol 305, 567-580.

718 Langfelder, K., Jahn, B., Gehringer, H., Schmidt, A., Wanner, G., and Brakhage, A.A.
719 (1998). Identification of a polyketide synthase gene (*pksP*) of *Aspergillus fumigatus*
720 involved in conidial pigment biosynthesis and virulence. Med Microbiol Immunol 187,
721 79-89.

722 Langfelder, K., Philippe, B., Jahn, B., Latge, J.P., and Brakhage, A.A. (2001).
723 Differential expression of the *Aspergillus fumigatus pksP* gene detected *in vitro* and *in*
724 *vivo* with green fluorescent protein. Infect Immun 69, 6411-6418.

725 Levitz, S.M., and Farrell, T.P. (1990). Human neutrophil degranulation stimulated by
726 *Aspergillus fumigatus*. J Leukoc Biol 47, 170-175.

727 Lim, K., Hyun, Y.-M., Lambert-Emo, K., Capece, T., Bae, S., Miller, R., Topham, D.J.,
728 and Kim, M. (2015). Neutrophil trails guide influenza-specific CD8⁺ T cells in the
729 airways. Science 349.

730 Lorincz, A.M., Timar, C.I., Marosvari, K.A., Veres, D.S., Otrokocsi, L., Kittel, A., and
731 Ligeti, E. (2014). Effect of storage on physical and functional properties of
732 extracellular vesicles derived from neutrophilic granulocytes. J Extracell Vesicles 3,
733 25465.

734 Lothar, J., Breitschopf, T., Krappmann, S., Morton, C.O., Bouzani, M., Kurzai, O.,
735 Gunzer, M., Hasenberg, M., Einsele, H., and Loeffler, J. (2014). Human dendritic cell
736 subsets display distinct interactions with the pathogenic mould *Aspergillus fumigatus*.
737 Int J Med Microbiol 304, 1160-1168.

738 Maertens, J.A., Raad, I.I., Marr, K.A., Patterson, T.F., Kontoyiannis, D.P., Cornely,
739 O.A., Bow, E.J., Rahav, G., Neofytos, D., Aoun, M., et al. (2016). Isavuconazole
740 versus voriconazole for primary treatment of invasive mould disease caused by
741 *Aspergillus* and other filamentous fungi (SECURE): a phase 3, randomised-
742 controlled, non-inferiority trial. Lancet 387, 760-769.

743 Majumdar, R., Tavakoli Tameh, A., and Parent, C.A. (2016). Exosomes mediate
744 LTB4 release during neutrophil chemotaxis. PLOS Biol 14, e1002336.

745 Marr, K.A., Schlamm, H.T., Herbrecht, R., Rottinghaus, S.T., Bow, E.J., Cornely,
746 O.A., Heinz, W.J., Jagannatha, S., Koh, L.P., Kontoyiannis, D.P., et al. (2015).
747 Combination antifungal therapy for invasive aspergillosis: a randomized trial. Ann
748 Intern Med 162, 81-89.

749 Matute, J.D., Arias, A.A., Wright, N.A., Wrobel, I., Waterhouse, C.C., Li, X.J.,
750 Marchal, C.C., Stull, N.D., Lewis, D.B., Steele, M., et al. (2009). A new genetic
751 subgroup of chronic granulomatous disease with autosomal recessive mutations in
752 p40 phox and selective defects in neutrophil NADPH oxidase activity. Blood 114,
753 3309-3315.

754 McCormick, A., Heesemann, L., Wagener, J., Marcos, V., Hartl, D., Loeffler, J.,
755 Heesemann, J., and Ebel, F. (2010). NETs formed by human neutrophils inhibit
756 growth of the pathogenic mold *Aspergillus fumigatus*. Microbes Infect 12, 928-936.

757 Mircescu, M.M., Lipuma, L., van Rooijen, N., Pamer, E.G., and Hohl, T.M. (2009).
758 Essential role for neutrophils but not alveolar macrophages at early time points
759 following *Aspergillus fumigatus* infection. *J Infect Dis* 200, 647-656.

760 Nieuwland, R., Berckmans, R.J., McGregor, S., Boing, A.N., Romijn, F.P.,
761 Westendorp, R.G., Hack, C.E., and Sturk, A. (2000). Cellular origin and procoagulant
762 properties of microparticles in meningococcal sepsis. *Blood* 95, 930-935.

763 Osherov, N., and Kontoyiannis, D.P. (2017). The anti-*Aspergillus* drug pipeline: Is the
764 glass half full or empty? *Med Mycol* 55, 118-124.

765 Patterson, T.F., Thompson, G.R., 3rd, Denning, D.W., Fishman, J.A., Hadley, S.,
766 Herbrecht, R., Kontoyiannis, D.P., Marr, K.A., Morrison, V.A., Nguyen, M.H., *et al.*
767 (2016). Practice Guidelines for the Diagnosis and Management of Aspergillosis: 2016
768 Update by the Infectious Diseases Society of America. *Clin Infect Dis* 63, e1-e60.

769 Petersen, T.N., Brunak, S., von Heijne, G., and Nielsen, H. (2011). SignalP 4.0:
770 discriminating signal peptides from transmembrane regions. *Nat Methods* 8, 785-786.

771 Piper, R.C., and Katzmann, D.J. (2007). Biogenesis and function of multivesicular
772 bodies. *Annu Rev Cell Dev Biol* 23, 519-547.

773 Pliyev, B.K., Kalintseva, M.V., Abdulaeva, S.V., Yarygin, K.N., and Savchenko, V.G.
774 (2014). Neutrophil microparticles modulate cytokine production by natural killer cells.
775 *Cytokine* 65, 126-129.

776 Priebe, S., Kreisel, C., Horn, F., Guthke, R., and Linde, J. (2015). FungiFun2: a
777 comprehensive online resource for systematic analysis of gene lists from fungal
778 species. *Bioinformatics* 31, 445-446.

779 Rossaint, J., Kuhne, K., Skupski, J., Van Aken, H., Looney, M.R., Hidalgo, A., and
780 Zarbock, A. (2016). Directed transport of neutrophil-derived extracellular vesicles
781 enables platelet-mediated innate immune response. *Nat Commun* 7, 13464.

782 Shlezinger, N., Irmer, H., Dhingra, S., Beattie, S.R., Cramer, R.A., Braus, G.H.,
783 Sharon, A., and Hohl, T.M. (2017). Sterilizing immunity in the lung relies on targeting
784 fungal apoptosis-like programmed cell death. *Science* 357, 1037.

785 Timar, C.I., Lorincz, A.M., Csepanyi-Komi, R., Valyi-Nagy, A., Nagy, G., Buzas, E.I.,
786 Ivanyi, Z., Kittel, A., Powell, D.W., McLeish, K.R., *et al.* (2013). Antibacterial effect of
787 microvesicles released from human neutrophilic granulocytes. *Blood* 121, 510-518.

788 Tkalcovic, J., Novelli, M., Phylactides, M., Iredale, J.P., Segal, A.W., and Roes, J.
789 (2000). Impaired immunity and enhanced resistance to endotoxin in the absence of
790 neutrophil elastase and cathepsin G. *Immunity* 12, 201-210.

791 Tsai, H.F., Chang, Y.C., Washburn, R.G., Wheeler, M.H., and Kwon-Chung, K.J.
792 (1998). The developmentally regulated alb1 gene of *Aspergillus fumigatus*: its role in
793 modulation of conidial morphology and virulence. *J Bacteriol* 180, 3031-3038.

794 Unkles, S.E., Valiante, V., Mattern, D.J., and Brakhage, A.A. (2014). Synthetic
795 biology tools for bioprospecting of natural products in eukaryotes. *Chem Biol* 21, 502-
796 508.

797 Vizcaino, J.A., Csordas, A., del-Toro, N., Dienes, J.A., Griss, J., Lavidas, I., Mayer,
798 G., Perez-Riverol, Y., Reisinger, F., Ternent, T., *et al.* (2016). 2016 update of the
799 PRIDE database and its related tools. *Nucleic Acids Res* 44, D447-456.

Walker, L., Sood, P., Lenardon, M.D., Milne, G., Olson, J., Jensen, G., Wolf, J.,
 Casadevall, A., Adler-Moore, J., and Gow, N.A.R. (2018). The viscoelastic properties
 of the fungal cell wall allow traffic of AmBisome as intact liposome vesicles. *MBio* 9.

Watanabe, J., Marathe, G.K., Neilsen, P.O., Weyrich, A.S., Harrison, K.A., Murphy,
 R.C., Zimmerman, G.A., and McIntyre, T.M. (2003). Endotoxins stimulate neutrophil
 adhesion followed by synthesis and release of platelet-activating factor in
 microparticles. *J Biol Chem* 278, 33161-33168.

Weidner, G., d'Enfert, C., Koch, A., Mol, P.C., and Brakhage, A.A. (1998).
 Development of a homologous transformation system for the human pathogenic
 fungus *Aspergillus fumigatus* based on the *pyrG* gene encoding orotidine 5'-
 monophosphate decarboxylase. *Curr Genet* 33, 378-385.

Wessel, D., and Flugge, U.I. (1984). A method for the quantitative recovery of protein
 in dilute solution in the presence of detergents and lipids. *Anal Biochem* 138, 141-
 143.

Yanez-Mo, M., Siljander, P.R., Andreu, Z., Zavec, A.B., Borrás, F.E., Buzas, E.I.,
 Buzas, K., Casal, E., Cappello, F., Carvalho, J., *et al.* (2015). Biological properties of
 extracellular vesicles and their physiological functions. *J Extracell Vesicles* 4, 27066.

Zarembek, K.A., Sugui, J.A., Chang, Y.C., Kwon-Chung, K.J., and Gallin, J.I. (2007).
 Human polymorphonuclear leukocytes inhibit *Aspergillus fumigatus* conidial growth
 by lactoferrin-mediated iron depletion. *J Immunol* 178, 6367-6373.

Legends to the Figures

Figure 1 *A. fumigatus* induces EVs release by human neutrophils.

(A) Time course of APB occurrence (green lines) and fungal-induced cell death (teal lines) at MOI 5:1 and 10:1. $n = 10(15)$ and $n = 12(17)$ for APB counts for MOI 5:1 and 10:1, respectively. $n = 4(20)$ and $n = 5(15)$ for viability data for MOI 5:1 and MOI 10:1, respectively. (B) Percentage of ABPs per total number of EVs. (C-E) Time course of total EV release and EV surface maturation markers (C) AnnV, (D) CD11b, and (E) CD63. Symbols represent significant differences between *pksP* afEVs (*pksP*) and wt afEVs (*), *pksP* afEVs (*pksP*), and sEVs (+), wt afEVs and sEVs (x). (C) $n = 27(40)$ for sEVs, $n = 16$ for wt afEVs and *pksP* afEVs; (D) $n = 23$ for sEVs, $n = 16$ for wt afEVs and *pksP* afEVs; (E) $n = 13$ for sEVs, $n = 9$ for wt afEVs and *pksP* afEVs. Data in (A and B-E) are presented as medians and interquartile range of absolute numbers of EVs per 10^7 PMNs. * $p < 0.05$, ** $p < 0.01$, *** $p < 0.001$ (Mann-Whitney test). (F-M) Cryo-TEM images of sEVs (F-I) and wt afEVs (J-M) 2 h post interaction. Representative images displaying sEVs (G-I) and wt afEVs (K-M) with different appearance. Scale bars correspond to 200 nm.

Figure 2 Core proteome cargo of PMN EVs.

Gene Ontology (GO)-term enrichment analysis of the core proteome cargo (60 proteins) that were shared between all groups of EVs (sEVs, wt afEVs, *pksP* afEVs). Data are representative of 2 technical replicates and were assigned to EV biogenesis by the FungiFun2 tool.

Figure 3 afEVs elicit fungistatic effects.

(A-D) Growth of fungal hyphae after 10 h of coincubation with afEVs derived from four different donors. afEVs were generated from PMNs infected with wt (EV (wt)) or *pksP* (EV (*pksP*)) conidia and coincubated with wt (+ wt) or *pksP* (+ *pksP*) conidia

using either single (1) or triple (3) doses of afEVs. The size of hyphae was assessed by automated analysis of 2D image data and results are displayed as median hyphae area in μm^2 in each field of view; data are represented as medians and interquartile range of the median hyphae area in each field of view; $n = 10$ fields of view per condition per time point. (E,F) Representative growth curves of wt and *pskP* fungal strains in presence and absence of afEVs for donor shown in (C). (G) Effects of sEVs on wt conidia compared to those of wt afEVs on wt conidia, $n = 3$ independent experiments, 20 fields of view per experiment per condition. * $p < 0.05$, ** $p < 0.01$, *** $p < 0.001$, p **** $p < 0.0001$ (Mann-Whitney test).

Figure 4 Effect of afEVs on hyphae.

(A) Density of wt afEVs and *pskP* afEVs inside and outside of wt and *pskP* mutant hyphae. (B) Estimation of hyphae-associated DNA signals (HADNA) in wild-type and *pskP* hyphae treated with wt afEVs and *pskP* afEVs, respectively, and non-treated control hyphae. Data in (A) and in (B) for EV groups derived from 3 independent experiments ($n = 13$ and 21 technical replicates for *pskP* and wt, respectively). Data in (B) for controls are representative of 1 experiment ($n = 5$ technical replicates). * $p < 0.05$, ** $p < 0.01$, *** $p < 0.001$ (Mann-Whitney test). (C) SEM of 50 h old cultures of wt (lower panel) treated with wt afEVs vs. healthy hyphae grown alone (upper panel). Samples were immobilized on filter membranes with a defined pore size of 5 μm (black circles). Scale bars are 50 μm . SEM images represent observations from two independent experiments with three technical replicates.

Figure 5 wt afEVs are internalized into the fungal cell wall and cytoplasm.

wt afEV internalization into fungi was analyzed by 3D quantitative analysis of Z-stacks with GFP-expressing *A. fumigatus* after 20 h of co-incubation. (A,B)

Representative cross-sections of Z-stacks showing lateral (X and Y) and axial (Z) dimensions of (A) a hyphae with internalized afEVs in red (Alexa-647), fungal cell wall in blue (CFW), and fungal cytoplasm in green (GFP) and corresponding control hyphae shown in (B). Scale bars represent 2 μ m. Image intensity was inverted. The darkest color corresponds to the highest fluorescence intensity. Histograms display specificity of signal of Alexa 647 dye used to stain afEVs. As seen in the control Z-stack, there is unspecific Alexa staining likely due to dye aggregation. (C) Schematic diagram of a cross-section of hyphae and different stages of afEV internalization. afEVs were located in 4 areas as indicated by the graphical representation. (D) Overview from the 3D image analysis of different locations of afEVs. Data are representative of 3 independent experiments with a total of 25 Z-stacks.

Figure 6 Intracellular production of human azurocidin and cathepsin G proteins in *A. fumigatus*.

(A) *A. fumigatus* wt and mutant strains Afazuro and AfcathG harboring the human azurocidin and cathepsin G gene, respectively, under the control of the tet^{ON} promoter. Cultures were grown for 24 h in the absence or presence of doxycycline. (B) Biomass measurement of wt and *A. fumigatus* mutant strains Afazuro and AfcathG with and without doxycycline. Data are representative of 3 independent experiments with three technical replicates. * $p < 0.05$, ** $p < 0.01$, *** $p < 0.001$ (Mann-Whitney test). (C) Detection of produced proteins in the *A. fumigatus* mutant strains. Bar plot shows the abundance level of the azurocidin protein in the case of the Afazuro strain, and cathepsin G protein for AfcathG strain, based on the intensity of the precursor ion. Data are generated from three analytical replicates.

900 **TABLE 1 Examples of TMT ratios of differentially produced proteins in isolated**
 901 **afEVs *versus* sEVs. pksP, pksP afEVs; wt, wt afEVs**
 902
 903

Figure 1

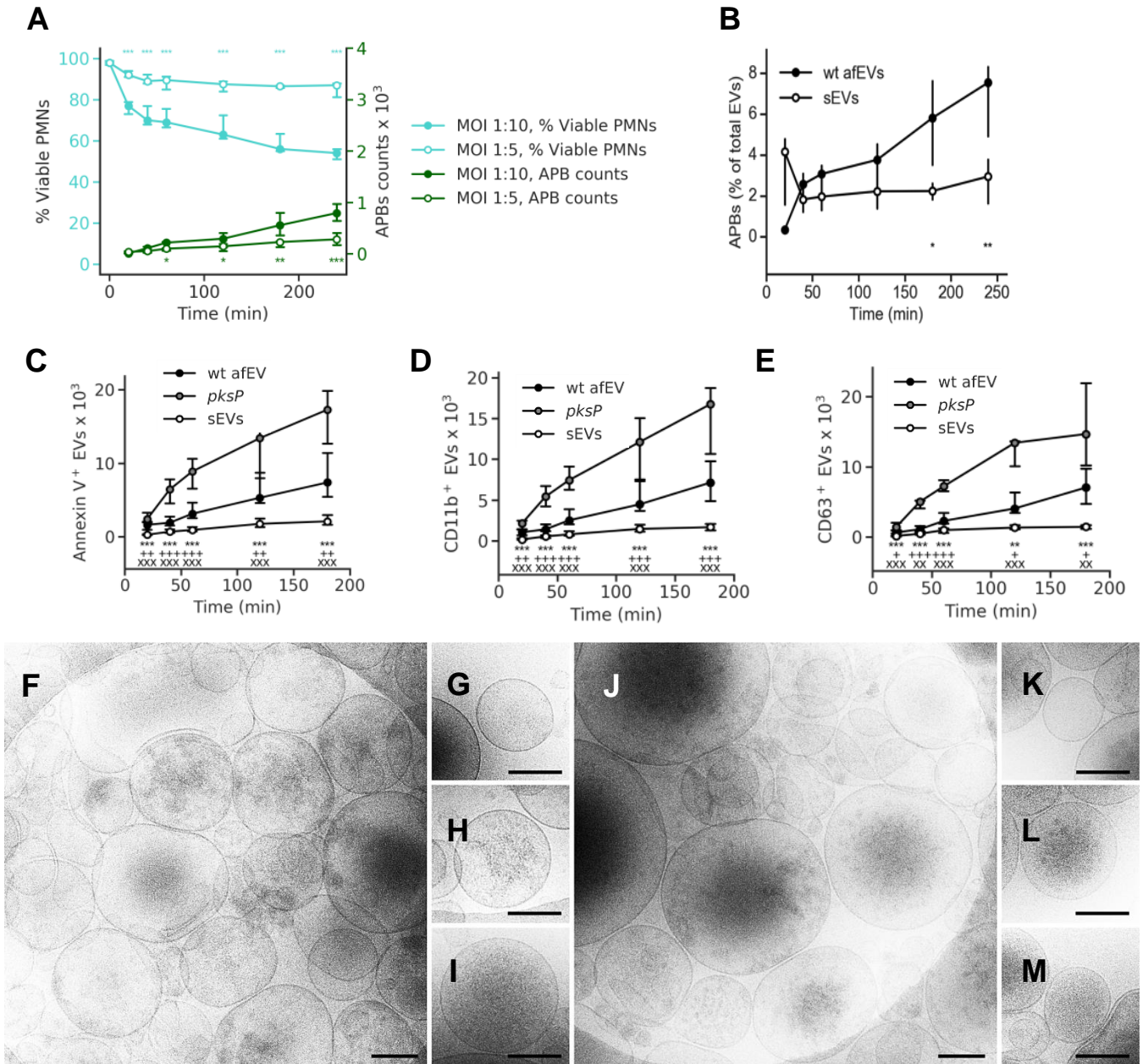


Figure 1 A. fumigatus induces EVs release by human neutrophils.

(A) Time course of APB occurrence (green lines) and fungal-induced cell death (teal lines) at MOI 5:1 and 10:1. $n = 10(15)$ and $n = 12(17)$ for APB counts for MOI 5:1 and 10:1, respectively. $n = 4(20)$ and $n = 5(15)$ for viability data for MOI 5:1 and MOI 10:1, respectively. (B) Percentage of ABPs per total number of EVs. (C-E) Time course of total EV release and EV surface maturation markers (C) AnnV, (D) CD11b, and (E) CD63. Symbols represent significant differences between *pksP* afEVs (*pksP*) and wt afEVs (*), *pksP* afEVs (*pksP*), and sEVs (+), wt afEVs and sEVs (x). (C) $n = 27(40)$ for sEVs, $n = 16$ for wt afEVs and *pksP* afEVs; (D) $n = 23$ for sEVs, $n = 16$ for wt afEVs and *pksP* afEVs; (E) $n = 13$ for sEVs, $n = 9$ for wt afEVs and *pksP* afEVs. Data in (A and B-E) are presented as medians and interquartile range of absolute numbers of EVs per 10^7 PMNs. * $p < 0.05$, ** $p < 0.01$, *** $p < 0.001$ (Mann-Whitney test). (F-M) Cryo-TEM images of sEVs (F-I) and wt afEVs (J-M) 2 h post interaction. Representative images displaying sEVs (G-I) and wt afEVs (K-M) with different appearance. Scale bars correspond to 200 nm.

Figure 2

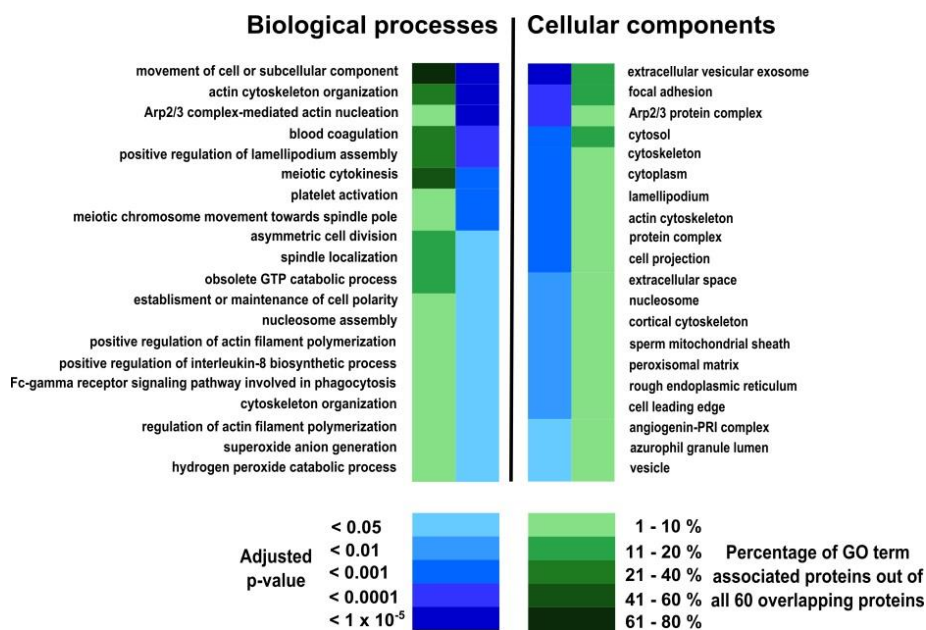


Figure 2 Core proteome cargo of PMN EVs.
Gene Ontology (GO)-term enrichment analysis of the core proteome cargo (60 proteins) that were shared between all groups of EVs (sEVs, wt afEVs, pksP afEVs). Data are representative of 2 technical replicates and were assigned to EV biogenesis by the FungiFun2 tool.

Figure 3

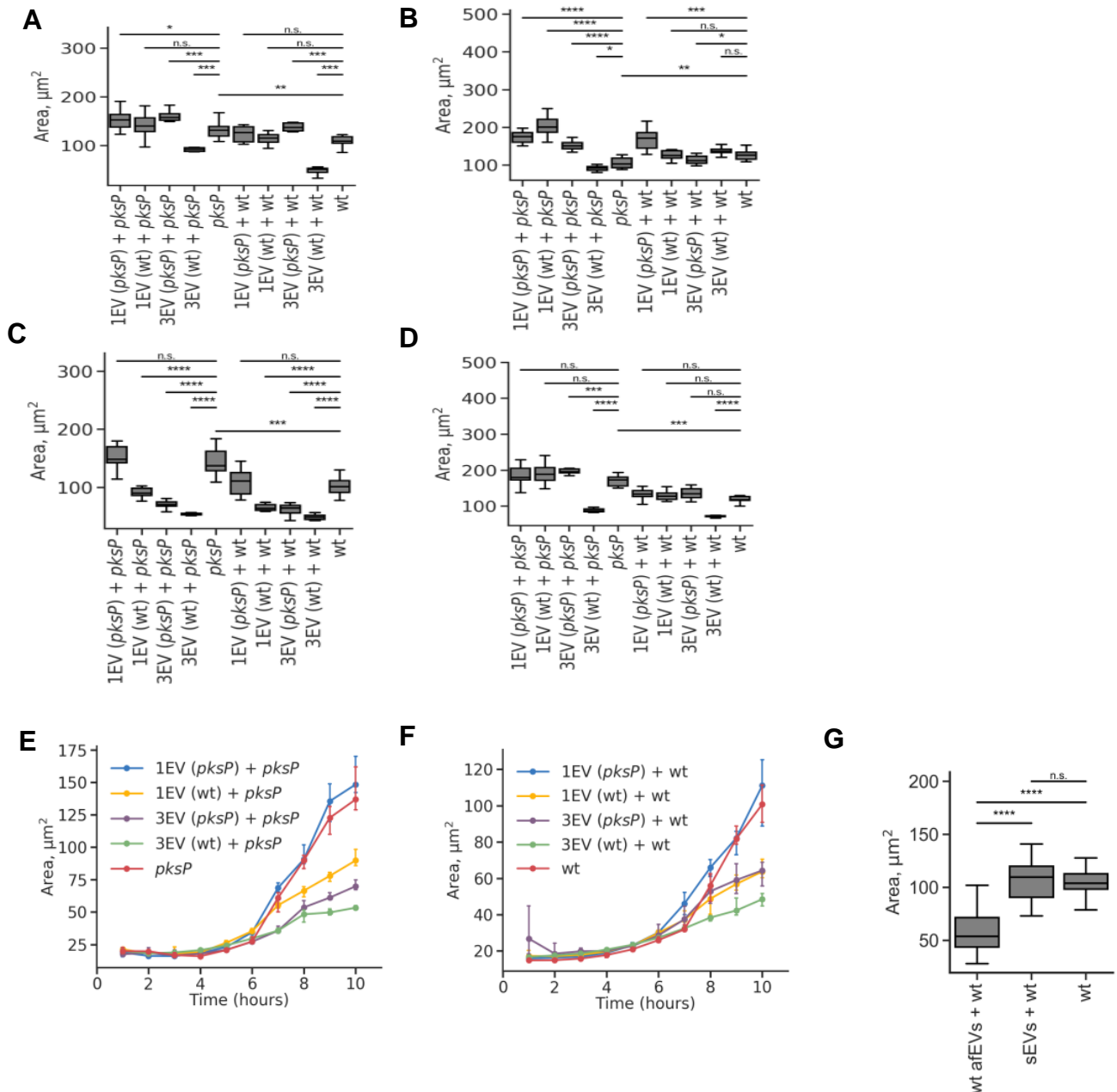


Figure 3 afEVs elicit fungistatic effects.

(A-D) Growth of fungal hyphae after 10 h of coincubation with afEVs derived from four different donors. afEVs were generated from PMNs infected with wt (EV (wt)) or *pksP* (EV (*pksP*)) conidia and coincubated with wt (+ wt) or *pksP* (+ *pksP*) conidia using either single (1) or triple (3) doses of afEVs. The size of hyphae was assessed by automated analysis of 2D image data and results are displayed as median hyphae area in μm^2 in each field of view; data are represented as medians and interquartile range of the median hyphae area in each field of view; n = 10 fields of view per condition per time point. (E,F) Representative growth curves of wt and *pksP* fungal strains in presence and absence of afEVs for donor shown in (C). (G) Effects of sEVs on wt conidia compared to those of wt afEVs on wt conidia, n = 3 independent experiments, 20 fields of view per experiment per condition. * p < 0.05, ** p < 0.01, *** p < 0.001, **** p < 0.0001 (Mann-Whitney test).

Figure 4

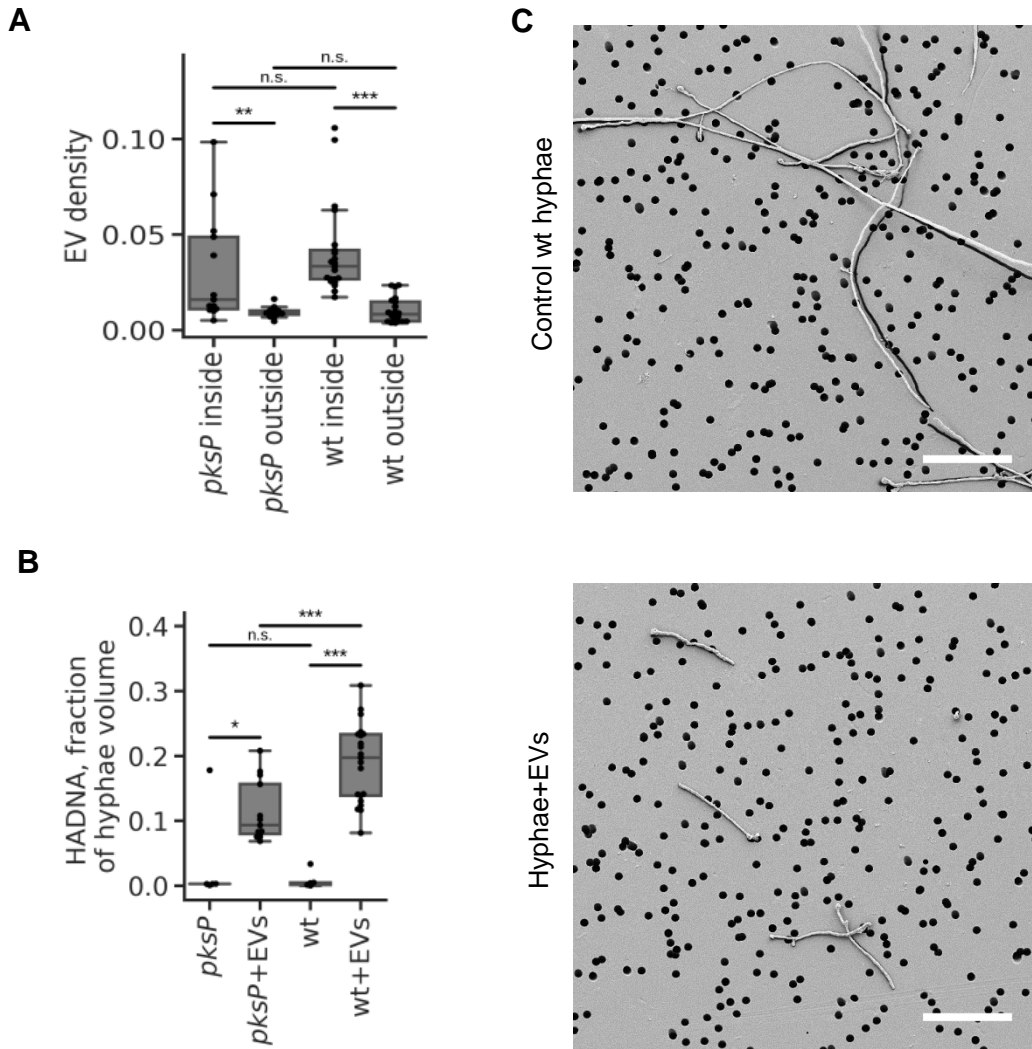


Figure 4 Effect of afEVs on hyphae.

(A) Density of wt afEVs and *pksP* afEVs inside and outside of wt and *pksP* mutant hyphae. (B) Estimation of hyphae-associated DNA signals (HADNA) in wild-type and *pksP* hyphae treated with wt afEVs and *pksP* afEVs, respectively, and non-treated control hyphae. Data in (A) and in (B) for EV groups derived from 3 independent experiments ($n = 13$ and 21 technical replicates for *pksP* and wt, respectively). Data in (B) for controls are representative of 1 experiment ($n = 5$ technical replicates). * $p < 0.05$, ** $p < 0.01$, *** $p < 0.001$ (Mann-Whitney test). (C) SEM of 50 h old cultures of wt (lower panel) treated with wt afEVs vs. healthy hyphae grown alone (upper panel). Samples were immobilized on filter membranes with a defined pore size of 5 μm (black circles). Scale bars are 50 μm . SEM images represent observations from two independent experiments with three technical replicates.

Figure 5

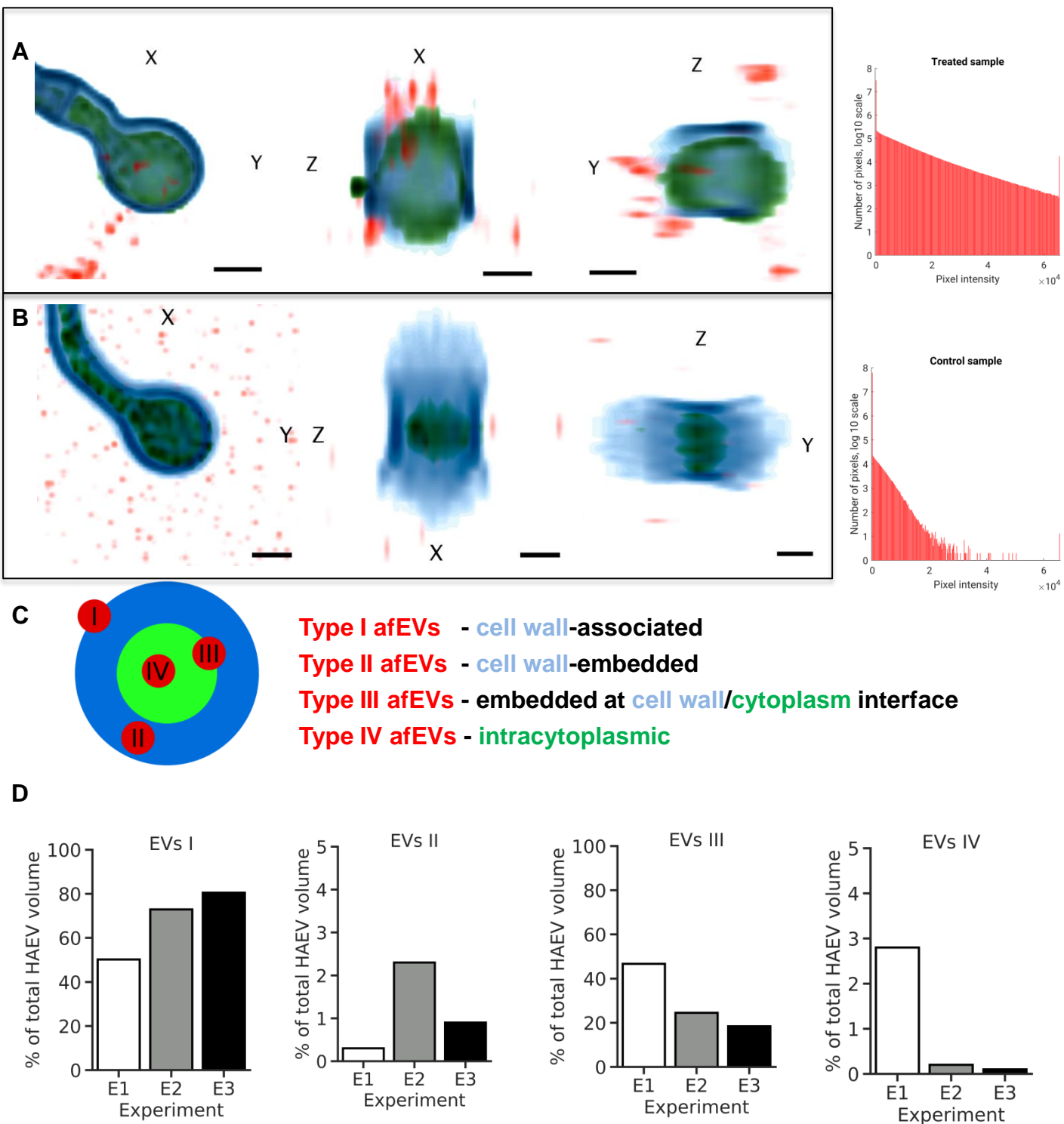


Figure 5 wt afEVs are internalized into the fungal cell wall and cytoplasm.

wt afEV internalization into fungi was analyzed by 3D quantitative analysis of Z-stacks with GFP-expressing *A. fumigatus* after 20 h of co-incubation. (A,B) Representative cross-sections of Z-stacks showing lateral (X and Y) and axial (Z) dimensions of (A) a hyphae with internalized afEVs in red (Alexa-647), fungal cell wall in blue (CFW), and fungal cytoplasm in green (GFP) and corresponding control hyphae shown in (B). Scale bars represent 2 μ m. Image intensity was inverted. The darkest color corresponds to the highest fluorescence intensity. Histograms display specificity of signal of Alexa 647 dye used to stain afEVs. As seen in the control Z-stack, there is unspecific Alexa staining likely due to dye aggregation. (C) Schematic diagram of a cross-section of hyphae and different stages of afEV internalization. afEVs were located in 4 areas as indicated by the graphical representation. (D) Overview from the 3D image analysis of different locations of afEVs. Data are representative of 3 independent experiments with a total of 25 Z-stacks.

Figure 6

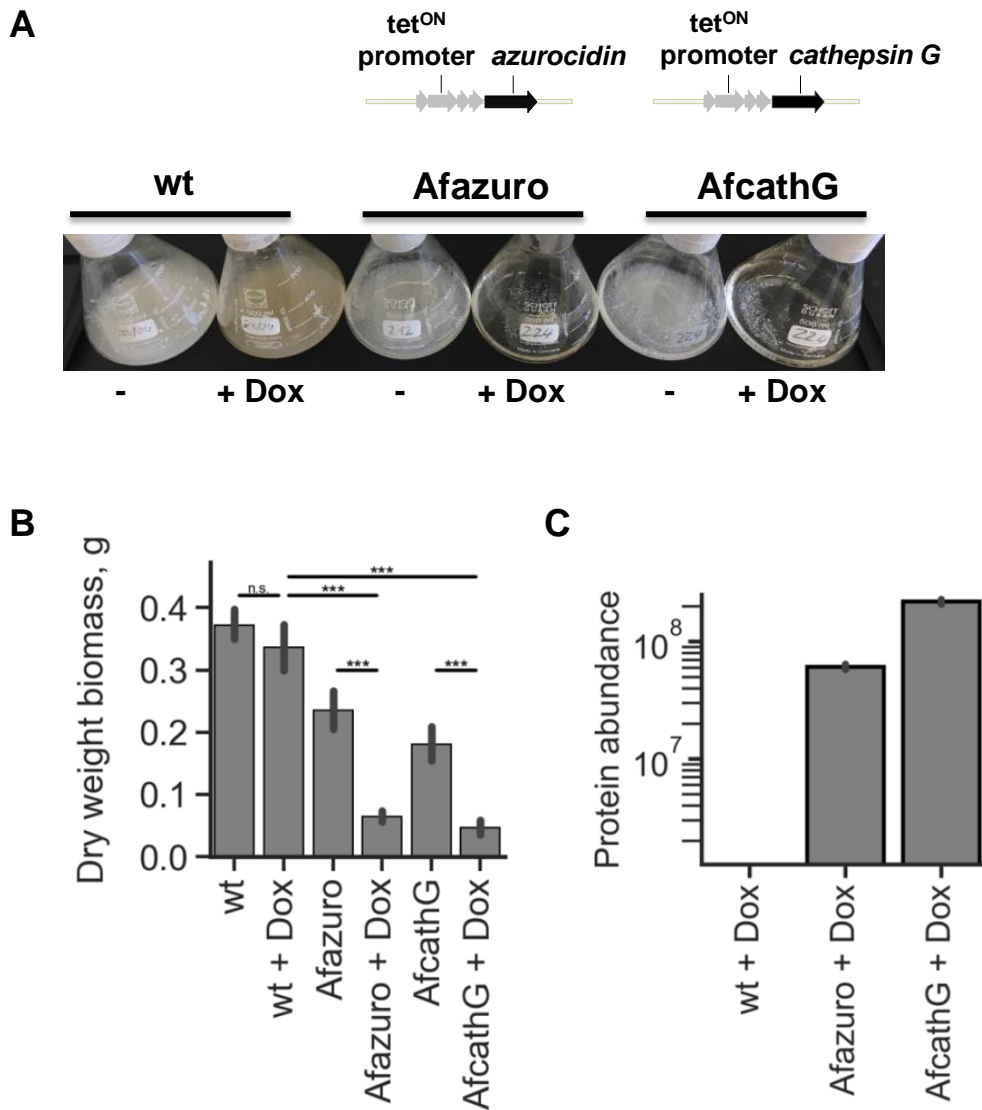


Figure 6 Intracellular production of human azurocidin and cathepsin G proteins in *A. fumigatus*. (A) *A. fumigatus* wt and mutant strains Afazuro and AfcathG harboring the human azurocidin and cathepsin G gene, respectively, under the control of the tet^{ON} promoter. Cultures were grown for 24 h in the absence or presence of doxycycline. (B) Biomass measurement of wt and *A. fumigatus* mutant strains Afazuro and AfcathG with and without doxycycline. Data are representative of 3 independent experiments with three technical replicates. * $p < 0.05$, ** $p < 0.01$, *** $p < 0.001$ (Mann-Whitney test). (C) Detection of produced proteins in the *A. fumigatus* mutant strains. Bar plot shows the abundance level of the azurocidin protein in the case of the Afazuro strain, and cathepsin G protein for AfcathG strain, based on the intensity of the precursor ion. Data are generated from three analytical replicates.

TABLE 1 Examples of TMT ratios of differentially regulated proteins in isolated afEVs *versus* sEVs. pksP, pksP afEVs; wt, wt afEVs

UniProt Accession	Protein	TMT ratio pksP afEVs/wt afEVs	TMT ratio wt afEVs/sEVs	TMT ratio pksP afEVs/sEVs
A0A0U1RRH7	Histone H2A	1.32	14.08	18.55
U3KQK0	Histone H2B	1.12	6.27	7.04
P68431	Histone H3.1	0.82	16.84	13.79
P08246	Neutrophil elastase	0.62	4.64	2.86
P05164	Myeloperoxidase	1.19	2.16	2.57
P08311	Cathepsin G	0.73	3.07	2.24
P59665	Defensin 1	2.04	13.41	27.37
P11215	CD11b (Integrin alpha M)	0.85	3.49	2.95
P08962	CD63	1.06	4.99	5.31
A0A087WVM2	CD177	0.88	2.72	2.40

A

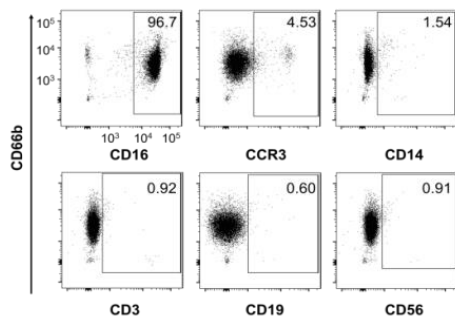
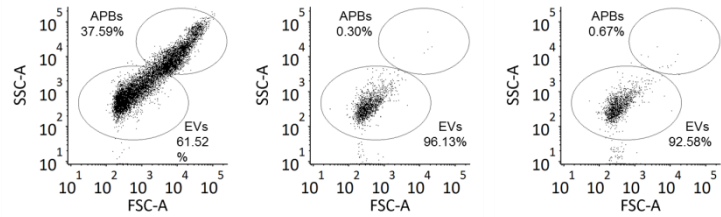
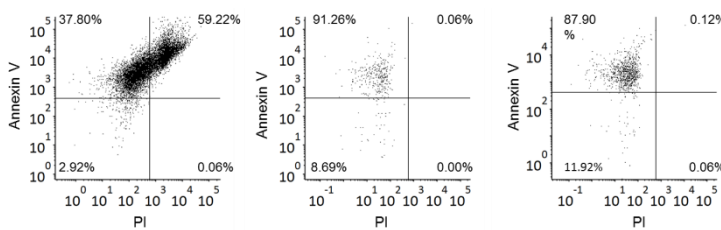


Figure S1

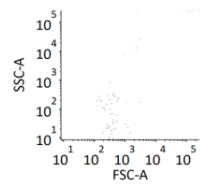
B



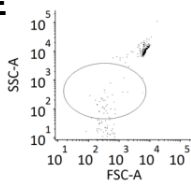
C



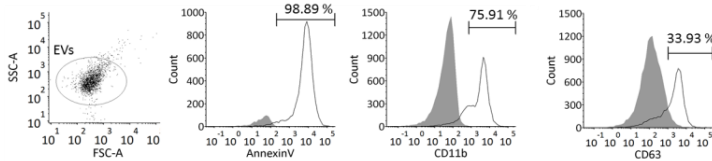
D



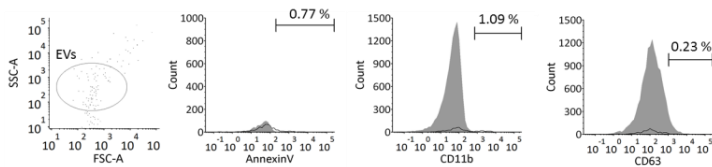
E



F



G

**Figure S1 Flow cytometry analysis of PMN EVs.**

(A) Purity of human PMNs used to generate PMN EVs. Purity was assessed by flow cytometry based on staining for CD66b⁺CD16⁺ PMNs, CCR3⁺ eosinophils, CD14⁺ monocytes, CD3⁺ T cells, CD19⁺ B cells, CD56⁺ NK, and NKT cells. The predominating contaminating fraction of cells were eosinophils. (B-C) Analysis of APBs defined as double positive AnnV⁺/PI⁺ EVs. PMNs cultured for 3 days on DMEM medium at 37°C were used as positive control for apoptosis (left panel). Two donors are shown in the center and right panel. (D-E) Flow cytometry protocol for phenotyping afEVs. (D) The instrumental background noise by pure HBSS is recorded and subsequently subtracted from all samples. (E) Mid-intensity rainbow beads of size 3.8 μ m are recorded to set the upper detection limit; afEVs are detected in the gate above the noise and below the beads in (E). Single-stained afEVs with the corresponding isotype Abs were used as negative controls in (F) and (G). Stained afEV suspensions were measured before (F) and after (G) detergent treatment with 1% (v/v) Triton X-100 to verify the vesicular nature of detected events. False positive events (detergent resistant) are subtracted from the results.

Figure S2

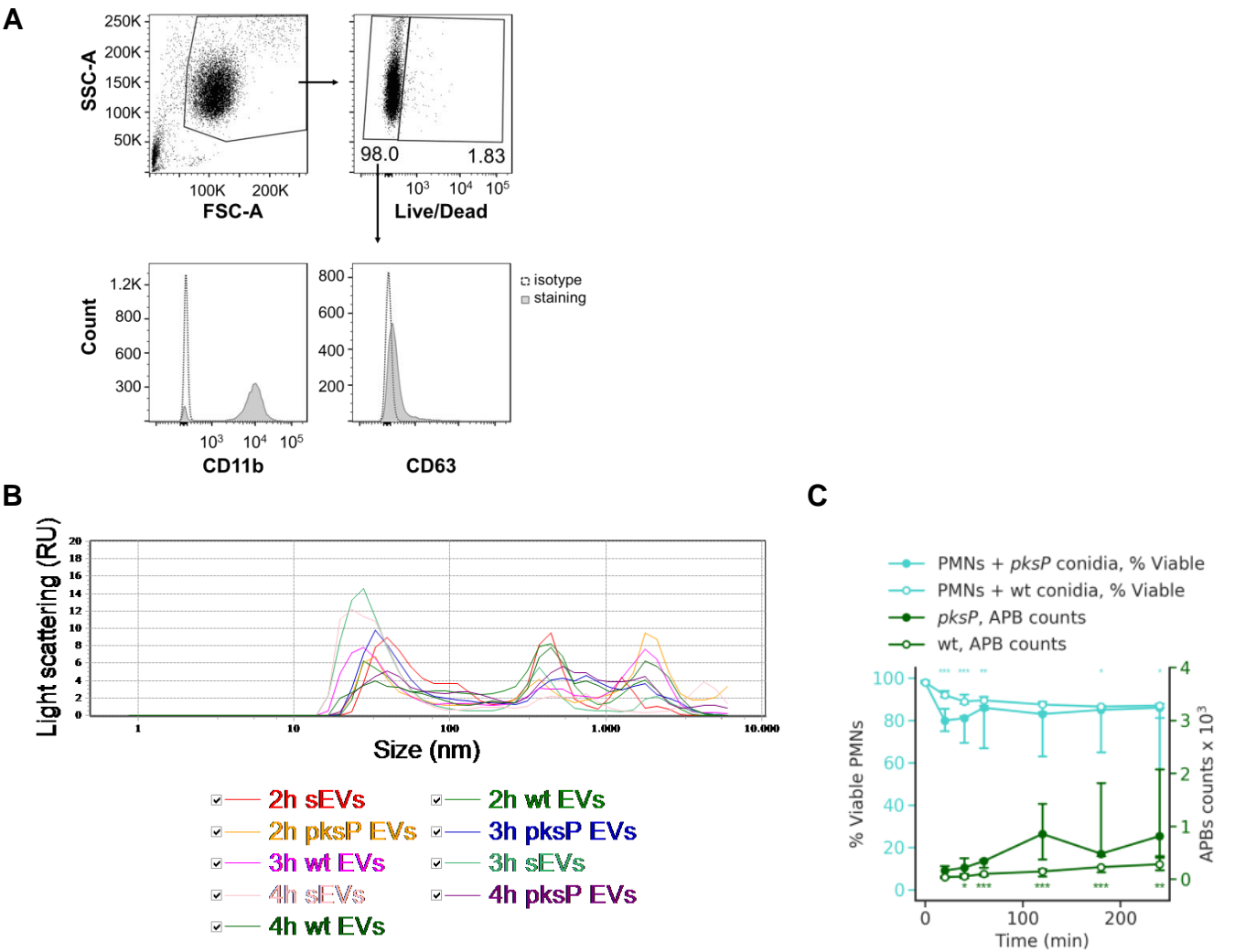


Figure S2 Characterization of afEV surface markers by flow cytometry.

(A) Flow cytometry measurement of PMN surface marker dynamics of CD11b and CD63 during infection with wt and *pksP* conidia at an MOI 5:1. PMNs were gated according to FSC/SSC properties, dead cells were excluded by staining with viability Zombie Dye, and expression of CD11b and CD63 was analyzed with FlowJo software (Tree Star). (B) Size distribution of afEVs (wt EVs = wt afEVs; pksP EVs = *pksP* afEVs) and sEVs generated at different time points measured by DLS. Data are representative of 3 independent experiments. (C) The time course of APB occurrence (green lines) in sEVs or afEVs group compared to that of spontaneous or fungus-induced cell death (teal lines). Data are represented as medians and interquartile range. Data for EVs are shown as absolute or relative vesicle numbers per 10⁷ PMNs. * $p < 0.05$, ** $p < 0.01$, *** $p < 0.001$ (Mann-Whitney test).

Figure S3

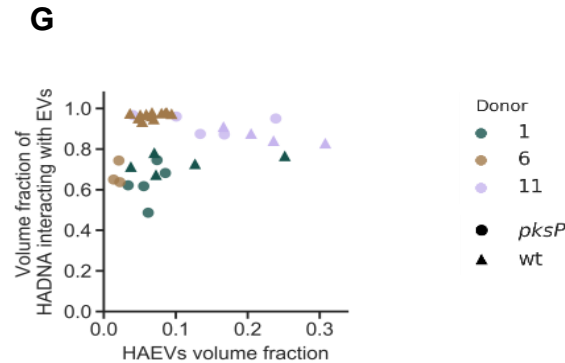
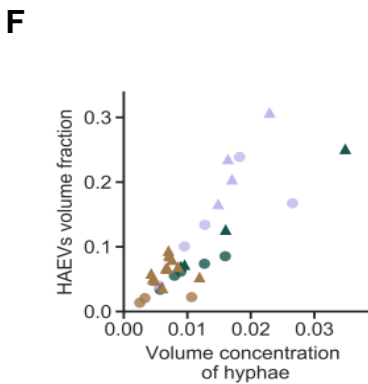
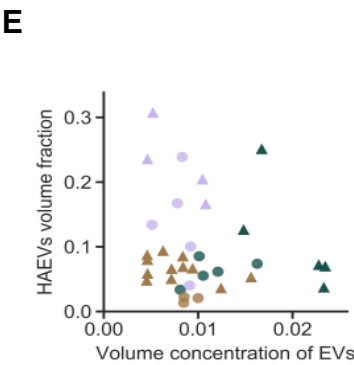
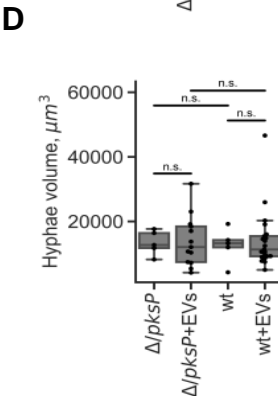
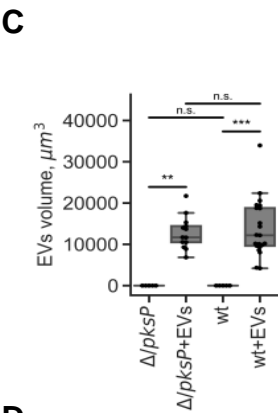
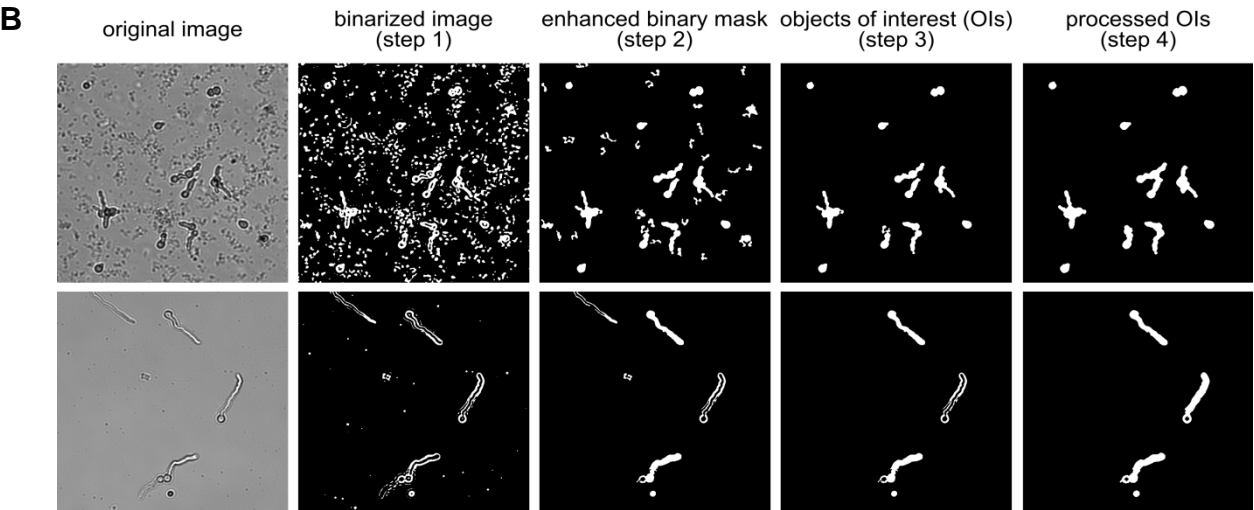
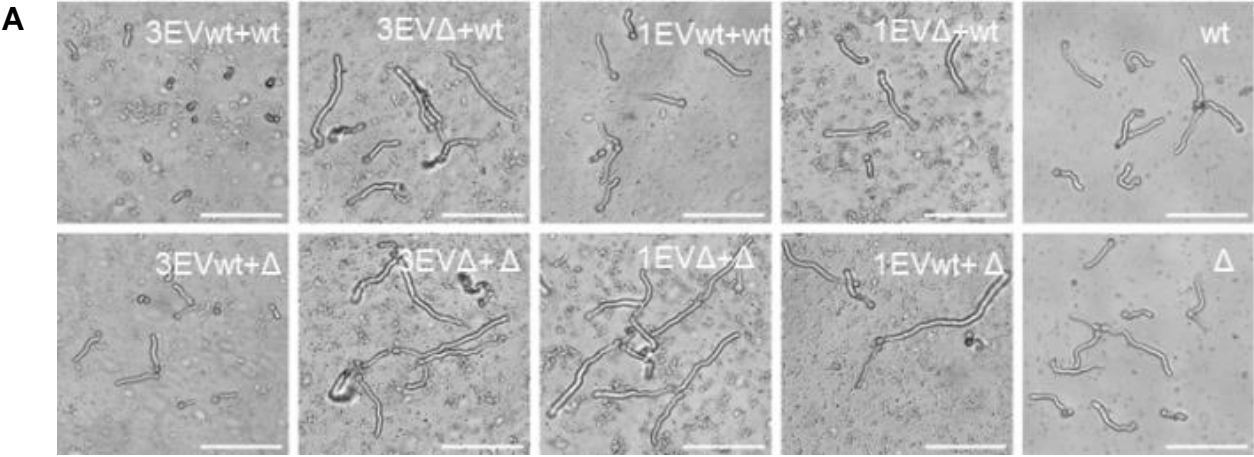


Figure S3

Figure S3 Effect of afEVs on fungal cells.

(A) Representative bright field images after 10 h of incubation of fungi with wt afEVs (EVwt) and *pksP* afEVs (EV Δ) on wt hyphae (+wt) and *pksP* mutant hyphae (+ Δ). Control, hyphae without EVs. The concentration of EVs was measured in “doses”. One dose of EVs was defined as the number of afEVs produced by 10^7 PMNs infected with *pksP* mutant conidia (see results). (B) Segmentation steps of an automated algorithm for 2D image analysis of fungal growth with (top rows) and without (bottom rows) afEVs. Scale bars are 20 μ m. Equal volumes of (C) EVs and (D) hyphae for wt and *pksP* samples were analyzed. (E) Dependence of the volume fraction of the hyphae-associated afEVs (HAEVs) (volume of HAEVs divided by the total afEV volume) on the volume concentration of afEVs (total afEV volume divided by the sample volume). (F) Dependence of the volume fraction of HAEVs on the volume concentration of hyphae (hyphae volume divided by the sample volume). (G) Dependence of the volume fraction of the hyphae-associated DNA (HADNA) that interacts with EVs on the volume fraction of HAEVs.

Figure S4

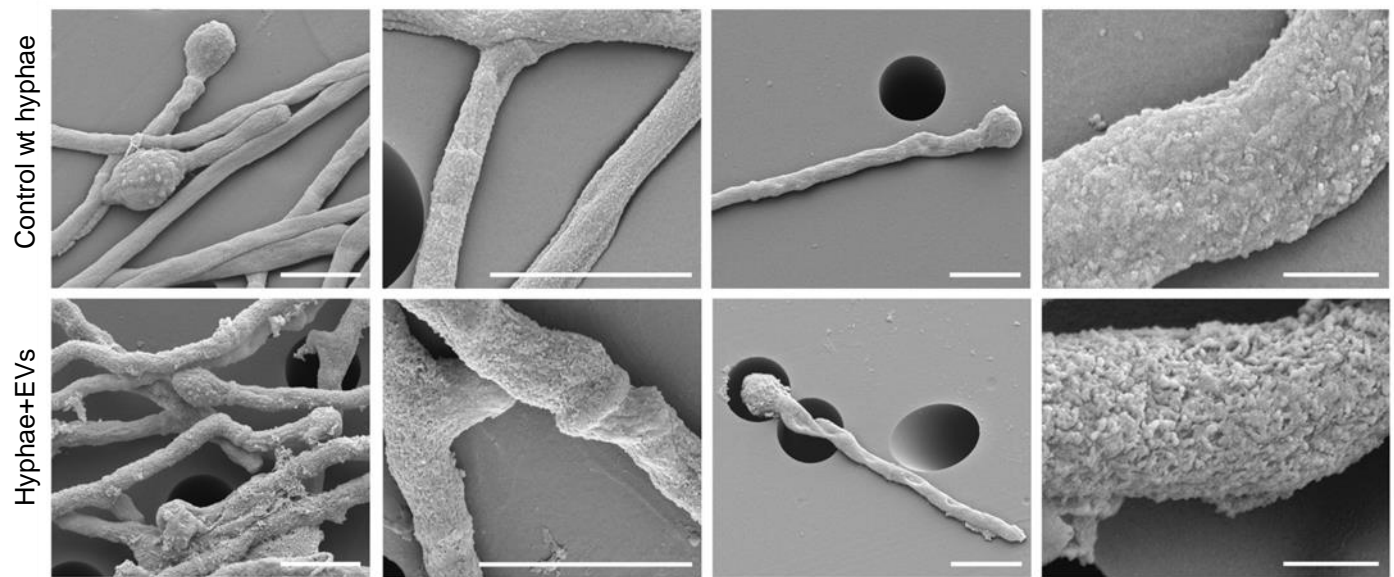
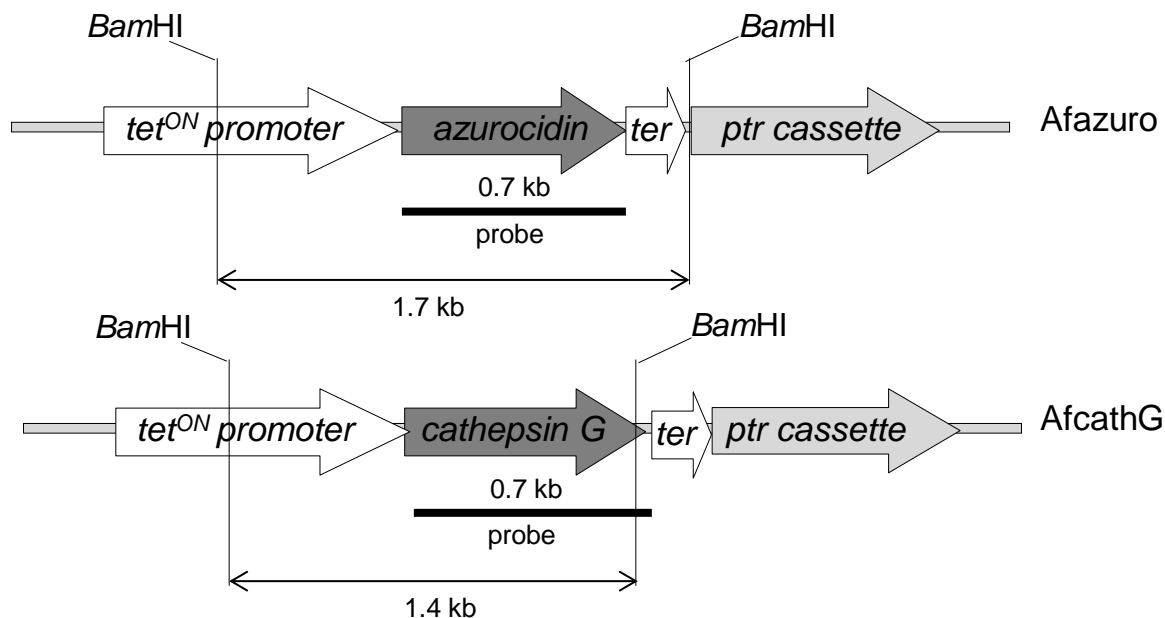


Figure S4 SEM imaging of wt afEV-treated hyphae.

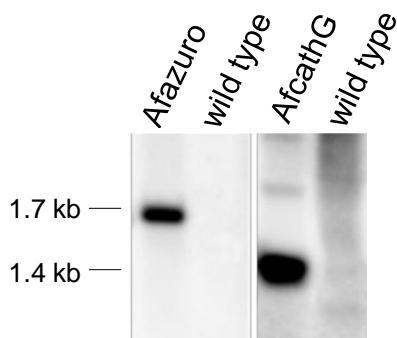
SEM of 50 h old cultures of wt (lower panel) treated with wt afEVs vs. healthy hyphae grown alone (upper panel). Samples were immobilized on filter membranes with a defined pore size of 5 µm (as seen in the overview images). The scale bar on the far-right panels is 1 µm. Scale bars on all other images are 5 µm. SEM images represent observations from 3 technical replicates, 2 independent experiments.

Figure S5

A



B



C

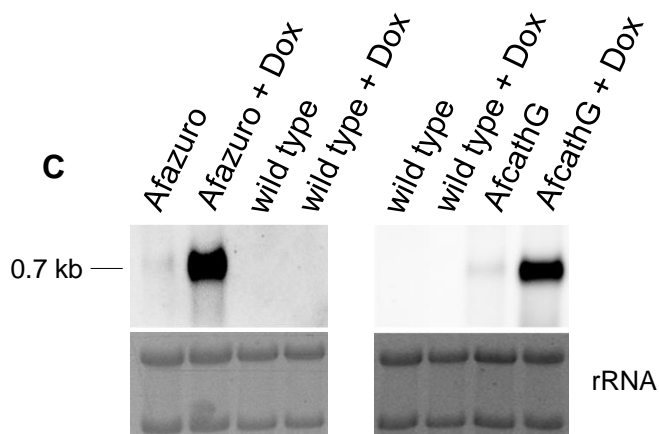


Figure S5 Verification of *A. fumigatus* transgenic strains expressing human azurocidin (Afazuro) and cathepsin G (AfcathG).

(A) Schematic of the predicted *Bam*HI restriction sites in the genome of the mutant strains following integration of the constructs used to express the human genes in the parental strain. *tet^{ON}* promoter, azurocidin-encoding gene, cathepsin G-encoding gene, *ter* (terminator), *ptr* cassette (pyrithiamine resistance marker). (B) Southern blot for confirmation of construct integration into the *A. fumigatus* genome. In the transgenic strains, a band with the expected size of 1.7 kb for the Afazuro strain, and 1.4 kb for the AfcathG strain, were observed. No signal was detected for the non transformed wild type. (C) Northern blot showing mRNA expression of azurocidin- and cathepsin G-encoding genes after induction of the *tet^{ON}* promoter with doxycycline (Dox).

Movies S1 Movie generation by using different dyes and reconstruction

Movie S2 afEVs localisation to four regions including the fungal cell wall and cytoplasm

Movie S3 Hyphae respond to afEVs by hyperbranching away from afEVs

Movies S1-3

3D surface reconstructions for image-based analysis of the interaction of afEVs with *A. fumigatus*. CLSM Z-stacks were captured 20 h post interaction. Cell wall chitin structures were stained with CFW (blue channel, movies S1-S3). DNA was stained with PI (red channel, movie S1,S3). AfEVs were stained with Annexin-V-FITC (green channel, movies S1, S3) or with Annexin-V Alexa 647 (red channel movie S2). In movie S2 the fungal cytoplasm contained GFP (green).

TABLE S1. Identified proteins with transmembrane domains predicted by SignalP, TMHMM and WoLF PSORT based on the here obtained TMT and LFQ data sets.

Accession	Protein	TMT dataset	LFQ dataset
P25024	C-X-C chemokine receptor type 1 (CXC-R1)	+	-
P25025	C-X-C chemokine receptor type 2 (CXC-R2)	+	-
Q9HDC9	Adipocyte plasma membrane-associated protein	+	+
P19397	Leukocyte surface antigen CD53	+	-
Q13724	Mannosyl-oligosaccharide glucosidase	+	-
J3KNB4	Cathelicidin antimicrobial peptide	+	-
P15144	Aminopeptidase N	+	+
Q14697	Neutral alpha-glucosidase AB	+	+
P08246	Neutrophil elastase	+	+
M9MML0	Fc of IgG low affinity IIIa receptor isoform 1	+	-
Q8TDB8	Solute carrier family 2, facilitated Glc transporter member 14	+	+
P27105	Erythrocyte band 7 integral membrane protein	+	+
P13498	Cytochrome b-245 light chain	+	+
P08962	CD63 antigen (Granulophysin)	+	-
P04839	Cytochrome b-245 heavy chain	+	-
P17213	Bactericidal permeability-increasing protein (BPI)	+	-
J3KPA1	Cysteine-rich secretory protein 3 CRISP3	+	+
Q53GQ0	Very-long-chain 3-oxoacyl-CoA reductase	-	+
Q96N66	Lysophospholipid acyltransferase 7 (LPLAT 7)	-	+
Q9NV96	Cell cycle control protein 50A	-	+
P08473	Neprilysin	-	+
O43760	Synaptogyrin-2	-	+
P07686	Beta-hexosaminidase subunit beta	-	+
P20701	Integrin alpha-L (CD11 antigen-like family member A)	-	+
F5H2F4	C-1-tetrahydrofolate synthase	-	+
P39656	Dolichyl-diphosphooligosaccharide-protein glycosyltransferase 48 kDa subunit	-	+
P00403	Cytochrome c oxidase subunit 2	-	+
P33121	Long-chain-fatty-acid--CoA ligase 1	-	+
Q15722	Leukotriene B4 receptor 1 (LTB4-R 1)	-	+
I3L0A0	HCG2044781	-	+
Q9NYU2	UDP-glucose:glycoprotein glucosyltransferase 1	-	+
Q8IWA5	Choline transporter-like protein 2	-	+
P13473	Lysosome-associated membrane glycoprotein 2 (LAMP-2)	-	+
Q7L5N7	Lysophosphatidylcholine acyltransferase 2	-	+
O75477	Erlin-1 (Endoplasmic reticulum lipid raft-associated protein 1)	-	+
P21730	C5a anaphylatoxin chemotactic receptor 1	-	+
E7ER45	Maltase-glucoamylase	-	+
P57088	Transmembrane protein 33	-	+

TABLE S2. Twenty most abundant proteins (PSMs/AAs) by TMT quantitation

Accession	Description	PSMs	AAs	PSMs/AAs
P05109	Protein S100-A8	5442	93	58.5
P06702	Protein S100-A9	4808	114	42.2
P80511	Protein S100-A12	992	92	10.8
C9JZR7	Actin, cytoplasmic 1 (Fragment)	913	103	8.9
P02788	Lactotransferrin	5929	710	8.4
P06899	Histone H2B type 1-J	912	126	7.2
P68871	Hemoglobin subunit beta	1039	147	7.1
P59665	Neutrophil defensin 1	650	94	6.9
P60709	Actin, cytoplasmic 1	2275	375	6.1
U3KQK0	Histone H2B	946	166	5.7
P07737	Profilin-1	767	140	5.4
P62736	Actin, aortic smooth muscle	1716	377	4.6
P62805	Histone H4	467	103	4.5
P08311	Cathepsin G	1155	255	4.5
P02042	Hemoglobin subunit delta	600	147	4.1
P04083	Annexin A1	1117	346	3.2
P05164-3	Isoform H7 of Myeloperoxidase	2324	777	3.0
P08246	Neutrophil elastase	752	267	2.8
P69905	Hemoglobin subunit alpha	367	142	2.6
P12429	Annexin A3	773	323	2.4

TABLE S3. Twenty most abundant proteins (PSMs/AAs) by label-free quantitation

Accession	Description	PSMs	AAs	PSMs/AAs
P06702	Protein S100-A9	3526	114	30.9
P05109	Protein S100-A8	2704	93	29.1
P59665	Neutrophil defensin 1	2710	94	28.8
P02788	Lactotransferrin	8015	710	11.3
P62805	Histone H4	920	103	8.9
P60709	Actin, cytoplasmic 1	2579	375	6.9
P68871	Hemoglobin subunit beta	940	147	6.4
P08311	Cathepsin G	1463	255	5.7
P68032	Actin, alpha cardiac muscle 1	2045	377	5.4
P69905	Hemoglobin subunit alpha	697	142	4.9
P05164-3	Isoform H7 of myeloperoxidase	3603	777	4.6
G3V1N2	HCG1745306, isoform CRA_a	435	110	4.0
P12429	Annexin A3	1222	323	3.8
P04083	Annexin A1	1175	346	3.4
P02042	Hemoglobin subunit delta	466	147	3.2
P07737	Profilin-1	425	140	3.0
P61626	Lysozyme C	385	148	2.6
Q562R1	Beta-actin-like protein 2	961	376	2.6
P20160	Azurocidin	640	251	2.5
X6R8F3	Neutrophil gelatinase-associated lipocalin	491	200	2.5

TABLE S4. List of primers used in this study.

Name	Sequence (5'- 3')
Azu_polictail_f	TCACCTCCATCTCAACTCCATCACATCACAATGATCGTCGGCGGCCGCAA
Azu_tefter_rev	TGAACAACCCCGGCCCTGATCAGTACTGACAATAAAAAAGATTCTTGTTT
Tef_ter_for	TCAGTACTGACAATAAAAAAG
Ura3_for	CCAGTAGATAGGGAGCCCTTG
Ura3_rev	CTGCTAACATCAAAAGGCCTC
pOlic_rev	CTCAACTCCATCACATCACA
cathG_polictail_f	TCACCTCCATCTCAACTCCATCACATCACAATGATCATCGGCGGCCGCGA
cathg_teftail_R	AGATGGAGACCCCTGTGATCAGTACTGACAATAAAAAAGATTCTTGTTT

Supplementary Methods: Human neutrophils produce antifungal extracellular vesicles against *Aspergillus fumigatus*

Iordana A. Shopova^{1,2}, Ivan Belyaev^{3,9}, Prasad Dasari⁴, Susanne Jahreis⁵, Maria C. Stroe^{1,2}, Zoltán Cseresnyés³, Anna Medyukhina³, Carl-Magnus Svensson³, Thomas Krüger², Viktória Szeifert⁶, Sandor Nietzsche⁷, Theresia Conrad⁸, Olaf Kniemeyer², Marie von Lilienfeld-Toal⁵, Peter F. Zipfel^{1,4}, Erzsébet Ligeti⁶, Marc Thilo Figge^{3,9} and Axel A. Brakhage^{1,2*}

¹Institute for Microbiology, Friedrich Schiller University, Jena, Germany

²Department of Molecular and Applied Microbiology, Leibniz Institute for Natural Product Research and Infection Biology (HKI), Jena, Germany

³Research Group Applied Systems Biology, Leibniz Institute for Natural Product Research and Infection Biology (HKI), Jena, Germany

⁴Department of Infection Biology, Leibniz Institute for Natural Product Research and Infection Biology (HKI), Jena, Germany

⁵Clinic of Internal Medicine II, Haematology and Oncology, University Hospital Jena, Germany,

⁶Department of Physiology, Semmelweis University, Budapest, Hungary,

⁷Centre for Electron Microscopy, Friedrich Schiller University, Jena, Germany

⁸Research Group Systems Biology and Bioinformatics, Leibniz Institute for Natural Product Research and Infection Biology (HKI), Jena, Germany

⁹Friedrich Schiller University, Jena, Germany

S1. CLSM setup

The imaging data were collected with a Zeiss LSM 780 confocal laser scanning microscope (Carl Zeiss SAS). Images were taken using either a 10x/NA 0.4 or a 20x/NA 0.7 objective lens in inverted configuration, resulting in a total magnification of 100x or 200x, respectively. In order to measure the point-spread function of the CLSM system, 5 μ l of the blue, green, and deep-red calibration beads from the PS-Speck Microscope Point Source Kit (diameter 170 nm; Invitrogen) were resuspended in the staining cocktail. The bead mixture was imaged under the same conditions as applied for the Z stacks of the hyphae-EV system. Individual 3D bead images were averaged per-color by HuygensPro and the resulting 3D bead images were used to distill the measured point-spread function for all three colors. For imaging hyphae and EVs, the CLSM objective lens and stage were preheated to 37°C for 3-5 h prior to image scanning. Bright field images were acquired from 10 different fields of view per well, once per hour for 15 time points using a 20x/NA 0.8 dry objective at 37°C, in 5% (v/v) CO₂ atmosphere.

For the Z-stacks, images were collected at an axial separation that was set according to the Nyquist criterion for the shortest wavelength, using the same Z step size for all channels. The axial range was adjusted to the thickness of the observed cells.

S2. Automated 2D image analysis of hyphal growth

The image data was saved in 16-bit CZI format and loaded into Matlab using the *bfoopen* script from the Open Microscopy Environment¹. The images were processed in five steps:

1. Binarization was performed using the function *imbinarize* from the Matlab ImageProcessing toolbox with the following parameters:

- threshold type: 'Adaptive';
- sensitivity factor for adaptive thresholding: 'Sensitivity'=0.45;
- foreground darker than background: 'ForegroundPolarity'='dark'.

2. Enhancement of the binary image included the following steps:

¹ <https://www.openmicroscopy.org/site/support/bio-formats5.3/developers/matlab-dev.html>

- *majority filter*: sets a pixel value to 1 if five or more pixels in its 3-by-3 neighborhood have values of 1; otherwise, the pixel value is set to 0;
- hole-filling inside ROI;
- object removal for ROI with area less than 200 pixels, which corresponds to the minimal area of resting conidia.

The resulting image is referred to as image *S*.

3. Selection of ROI:

- splitting of image *S* into two masks, *M* and *S'*, based on the object area: image *M* containing all ROI with an area less than 1000 pixels that correspond to resting, swollen and germinated conidia, as well as parts of vesicle clumps, and image *S'* with all remaining large ROI, corresponding to hyphae;
- removal of all ROI from mask *M* with solidity below 0.85, corresponding to vesicle clumps; the resulting mask is referred to as *M'*;
- combination of masks *M'* and *S'* into one mask *R* by the logical sum operation of *M'* and *S'*.

4. Image post-processing and filtering:

- morphological closing of the mask *R* with two “line”-elements (10 pixels long, orientation 45 and 135 degrees) to connect broken contours;
- removing all ROI that have the 1st percentile of their Feret diameters less than 17 pixels (the size of resting conidia); this removes the remaining vesicle clumps, which have regions thinner than 17 pixels; for the Feret diameters calculation the toolbox “Feret diameter and oriented box” was used (David Legland, <https://www.mathworks.com/matlabcentral/fileexchange/30402-feret-diameter-and-oriented-box>).

5. Area measurement of the ROI:

- the area of each object was computed using the function *regionprops* with the parameter 'FilledArea';
- the median of the areas of all ROI in an image was used to characterize fungal coverage in the image.